# Quiescence modulates stem cell maintenance and regenerative capacity in the aging brain

Kalamakis Georgios[1,2], Brüne Daniel[1], Ravichandran Srikanth[3], Bolz Jan[1], Fan Wenqiang[7,8], Ziebell Frederick[1,11], Stiehl Thomas[11], Catalá-Martinez Francisco[1], Kupke Janina[1], Zhao Sheng[1], Llorens-Bobadilla Enric[1], Bauer Katharina[12], Limpert Stefanie[1], Berger Birgit[1], Christen Urs[13], Schmezer Peter[14], Mallm Jan Philipp[15,16], Berninger Benedikt[7,8,9,10], Anders Simon[17*], Del Sol Antonio[3,4,5,6*], Marciniak-Czochra Anna[9*], Martin-Villalba Ana[1]

* Equal contribution

Lead contact: AMV a.martin-villalba@dkfz-heidelberg.de

[1]Molecular Neurobiology, German Cancer Research Center, 69120, Heidelberg, Germany.
[2]PhD student at University of Heidelberg, 69120, Heidelberg, Germany
[3]Luxembourg Centre for Systems Biomedicine, University of Luxembourg, 4362, Luxembourg.
[4]CIC bioGUNE, 48160, Derio, Spain.
[5]IKERBASQUE, Basque Foundation for Science, 48013, Bilbao, Spain
[6]Moscow Institute of Physics and Technology, 141700, Dolgoprudny, Russia
[7]Institute of Physiological Chemistry, University Medical Center Johannes Gutenberg University, 55128, Mainz, Germany.
[8]Focus Program Translational Neuroscience, Johannes Gutenberg University, 55122, Mainz, Germany.
[9]Institute of Psychiatry, Psychology & Neuroscience, Centre for Developmental Neurobiology King's College London, SE1 1UL, London, UK.
[10]Institute of Psychiatry, Psychology & Neuroscience, MRC Centre for Neurodevelopmental Disorders, King's College London, SE1 1UL, London, UK.
[11]Institute of Applied Mathematics, Interdisciplinary Center for Scientific Computing and Bioquant, Heidelberg University, 69120, Heidelberg, Germany.
[12]Heidelberg Center for Personalized Oncology (DKFZ-HIPO), German Cancer Research Center, 69120, Heidelberg, Germany.
[13]Goethe University Hospital Frankfurt / ZAFES, 60596, Frankfurt, Germany.
[14]German Cancer Research Center, Division of Epigenomics and Cancer Risk

Factors, 69120, Heidelberg, Germany.
[15]Division Chromatin Networks, German Cancer Research Center, 69120, Heidelberg, Germany.
[16]Single-cell Open Lab, German Cancer Research Center, 69120, Heidelberg, Germany.
[17]Center for Molecular Biology, Heidelberg University, 69120, Heidelberg, Germany.

**Summary**

The function of somatic stem cells declines with age. Understanding the molecular underpinnings of this decline is key to counteract age-related disease. Here, we report a dramatic drop in the neural stem cells (NSCs) number in the aging murine brain. We find that this smaller stem cell reservoir is protected from full depletion by an increase in quiescence that makes old NSCs more resistant to regenerate the injured brain. Once activated, however, young and old NSCs show similar proliferation and differentiation capacity. Single cell transcriptomics of NSCs indicated that aging changes NSCs minimally. In the aging brain niche-derived inflammatory signals and the Wnt antagonist sFRP5 induce quiescence. Indeed, intervention to neutralize them increased activation of old NSCs during homeostasis and following injury. Our study identifies quiescence as key feature of old NSCs imposed by the niche and uncovers ways to activate NSCs to repair the aging brain.

**Key words:**

Stem cell aging, neural stem cells, Quiescence, Inflammation, Wnt Signaling, single cell transcriptomics, modeling, simulations, interferon, sFRP5, subventricular zone.

## Introduction

In the adult murine brain, NSCs residing within the ventricular-subventricular zone (V-SVZ) of the lateral ventricles generate olfactory bulb (OB) interneurons required to fine-tune odor discrimination throughout the life of the animal. Recent studies have characterized the division mode and the transcriptional programs underlying the different activation states of NSCs in the young brain. Yet, whether this default program is affected by age and how this potentially influences NSC function is controversial. In the old brain NSCs retain the ability to generate the different subtypes of OB interneurons, albeit at much lower numbers (Basak et al., 2018; Dulken et al., 2017; Llorens-Bobadilla et al., 2015; Obernier et al., 2018; Shook et al.,

2012). Whereas some studies report a decreased proliferation of NSCs (Capilla-Gonzalez et al., 2014; Shi et al., 2017; Silva-Vargas et al., 2016), others report no changes or even an increase in proliferation (Ahlenius et al., 2009; Shook et al., 2012). In the human brain, generation of new neurons is debated (Kempermann et al., 2018). In the adult human brain C14 birth dating studies have revealed the existence of new neurons in the striatum, and the V-SVZ NSCs are regarded as the source of these striatal interneurons (Ernst et al., 2014).

The present study addresses the stem cell dynamics within the V-SVZ throughout the life of the animal. Mathematical modelling is used to explore how time-dependent changes in key stem cell features can explain the age-dependent decline of the NSC pool. Profiling of the single transcriptomes of young and aged NSCs and of the transcriptomes of neighboring niche cells is used to identify drivers of this age-dependent changes. Altogether, this study advances our understanding of the molecular underpinnings of age-related decline in NSC function.

## Results

### A time-dependent increase in quiescence maintains a stem cell reservoir at old age while making stem cells more resistant to activation

To assess age-related changes of NSCs, we quantified the numbers of NSCs and their immediate progeny across different ages. To this end, we performed FACS analysis of different cell subpopulations isolated from the V-SVZ of 2, 7 and 22 months old (MO) mice (Fig.1A, S6A). This analysis revealed that the total number of NSCs significantly declines between 2 and 7 MO and remains low at 22 MO. We further analyzed the numbers of quiescent NSCs (qNSCs), active NSCs (aNSCs) and transit amplifying progenitors (TAPs). All three populations showed similar dynamics, with a significant decrease from 2 to 7 MO, and low numbers from 7 to 22 MO. To confirm this observation, we quantified NSCs and their progeny within the V-SVZ *in situ*. The TLX-CreER$^{T2}$YFP reporter mouse line was used to label NSCs (Liu et al., 2010). To additionally identify progenitors that became quiescent at embryonic day 14 (E14) and only got reactivated in the adult V-SVZ (Fuentealba et al., 2015), we administered BrdU at E14. Note that every labeling protocol used in this study can be found in Fig.S5A. The number of embryonic-label retaining NSCs (E-LRCs) drastically decreased between 2 and 14 MO (Fig.1B,C). Together, these data show a rapid decline of the number of NSCs from 2 to 7 MO that slows down thereafter.

Others had reported this age-dependent decrease of NSC number, however the NSC features that have to change with time to explain this decline had not been addressed. To this end, we built a mathematical model (MM) of V-SVZ NSC dynamics (Data S1), based on a mathematical framework developed to describe adult hippocampal neurogenesis (Ziebell et al., 2018; 2014). For model fitting we considered a joint data set consisting of the subset of the frequency of active cells as a fraction of the adult label-retaining cells (LRCs- 14d BrdU administration in drinking water followed by 14d of chase time before sacrificing the animals at indicated ages; Fig.S5) and of the subset of active cells as a fraction of the TLX labeled cells (Fig.S1A-D, S5). We fitted the model using both subsets simultaneously. Based on our own experimental data and current literature (Basak et al., 2018; Obernier et al., 2018) we assumed that qNSCs can enter cell cycle to become aNSCs and give rise to either two qNSCs or two TAPs with the capacity of performing *n* symmetric self-renewing divisions (Fig.1D). This is different to the assumptions we used in our previous work on NSC dynamics in the hippocampus, where we allowed additional NSC fates, like asymmetric divisions or depletion through cell death or direct transformation into astrocytes (Ziebell et al., 2014; 2018).

First, we designed a model with cell parameters that do not change in time and evaluated its outcome by comparing it to experimental data. The assumption of time-constant parameters, called “no-aging” scenario, led to an exponential decay of the total NSC number, which did not match the experimental observation of saturation of the decline of NSC numbers at an older age (Fig.1E, left panel). Furthermore, contrary to the experimental data, the model with this assumption predicted that the fraction of active among all LRCs and TLX-labeled cells would not change over time (Fig.1E, right panel). To identify mechanisms that might explain the observed decline in the fraction of the active cells, we considered three age-dependent scenarios: increase in cell-cycle length; increase in self-renewal; and increase of the mean time spent in quiescence (Fig.1F-H, Data S1). To compare model predictions to experimental data, we examined the following time-dependent quantities: number of NSCs, and fraction of active among adult LRCs and TLX-labeled cells.

We first assumed, as previously suggested by (Daynac et al., 2016), that upon aging aNSCs require progressively more time to complete their cell cycle (without taking in account time in G0 phase). As in the no-aging scenario, this led to dynamics with faster depletion of the total number of NSCs (Fig.1F, left panel) and time-constant

fraction of aNSCs (Fig.1F, right panel). In the second scenario, we modeled an age-related increase of the fraction of self-renewal, i.e., assuming that upon aging a higher fraction of aNSCs divisions results in two qNSCs rather than two TAPs. This model correctly reproduced the saturation in the decay of the total number of NSCs (Fig.1G, left panel) but showed only a 3.5% decline in the fraction of aNSCs in contrast to the 37% decline observed in the experimental data and it would require a low fraction of aNSCs in young mice (Fig.1G, right panel). In addition, the model predicted a rapid decline in the number of NSCs at young age, which would require a much larger number of cells (1.1×10^6 cells) at the beginning of the process (Fig.S1E). Finally, we assumed that the time NSCs spend in quiescence (G0) increases with age. Changes in this feature fit the experimental data best, since they are not only showing the saturation of the decline in total NSC numbers (Fig.1H, left panel), but also the drop in the fraction of aNSCs (35% in the model simulation vs. 37% in the data) (Fig.1H, right panel). The conclusion that only the increasing quiescence scenario can explain the data is supported by the Akaike information criterion (AIC); (Data S1-Tables 1-3). To further validate our results, we considered a model with two time-dependent cell parameters accounting for both, simultaneous increase of the fraction of NSC self-renewal and increase of the mean time spent by a cell in quiescence. Although increasing the number of free parameters allows finding a fit that seems closer to the data, the model combining two time-dependent parameters was not superior in terms of AIC. To quantify the contribution of changes of both factors to the optimal fit, we extracted the dynamics of the two parameters from the model (Fig.S1F and Data S1-Tables 1-3). Comparison of the estimated cell properties in the different models showed that even if the two parameters undergo age-dependent changes, the major component of the regulatory process that explains the observed dynamics, is the increase in time spent in quiescence (decreasing rate of activation from quiescence). This prediction was experimentally validated by the significant decrease of the percentage of aNSCs among E-LRCs between 2, 7 and 14 MO (Fig.1I, S1G). Altogether, these data show, that during homeostasis the fraction of NSCs in quiescence increases with age.

We next asked if qNSCs are equally able to become activated upon injury in the young and old brain. To this end we ablated cycling cells including aNSCs, TAPs and NBs using temozolomide (TMZ), a DNA-alkylating agent (Fig.2A). This ablation

activates qNSCs to replenish the NSC compartment (Mich et al., 2014). Proliferation of V-SVZ NSCs in 2 and 22 MO mice was assessed by a 2-hour BrdU labeling protocol at 0, 1, 9 and 35 days following TMZ treatment (Fig.S2A, S5). 35 days following TMZ treatment, the number of aNSCs rose again to about the same level as before (92% of the cell number after the control treatment; CI95:67%-117%) in young mice, while only 44% (CI95:37%-51%; p=2.7*10^-5) of the control level was achieved in old mice (CI95=95% confidence interval according to Student's t-test) (Fig.2B). Hence, old qNSCs are more resistant to injury-induced activation and thus unable to quickly repair the old brain.

**Young and old NSCs are functionally and molecularly similar**

We next set out to address the factors involved in the NSCs' resistance to enter the activation state. DNA damage increases upon aging in several stem cell compartments (Oh et al., 2014), potentially compromising their function. This is the case for quiescent hematopoietic stem cells (HSCs) that exhibit DNA damage upon repeated activation, as assessed by the alkaline comet assay (Walter et al., 2015). However, the comet assay on freshly sorted qNSCs and aNSCs from young and old mice revealed no major differences in the levels of DNA damage (Fig.S2B,C, S6). We next tested if once activated, old and young NSCs would perform different. To this end, we recorded the cell dynamics of freshly sorted active NSCs from 2 and 22 MO mice via time-lapse video microscopy for a period of 6 days and reconstructed their lineage trees (Fig.2C, S2D). In the absence of growth factors or other extrinsic signals, aNSCs follow their *in vivo* fate allowing evaluation of parameters such as clone size, rounds of division and average cell cycle length (Ortega et al., 2013). After several rounds of division, both young and old aNSCs gave rise to neuroblasts (NBs) demonstrating their neurogenic potential (Fig.2C); both young and old aNSCs generated clones of similar size (Fig.2D), underwent similar number of division rounds (Fig.2E) and exhibited similar average cell cycle length (Fig.2F). In addition, freshly sorted aNSCs from 2, 7 and 22 MO mice exhibited similar self-renewal capacity as assessed by an *in vitro* sphere assay (Fig.S2E,F). Altogether, these results show that once activated, old NSCs perform as well as their younger counterparts.

We then investigated the molecular underpinnings of age-induced quiescence using single cell transcriptomics data of 92 NSCs from 2 MO mice and 133 NSCs from 23

MO mice. These NSCs were sequenced using the Smart-seq2 protocol. Our analysis on NSCs from young mice has already been published (Llorens-Bobadilla et al., 2015) (Fig.S6A). Here we used additional libraries from old mice that had also been prepared in the context of our previous study but not discussed there. When including these, hierarchical clustering identified the four different activation states of NSCs (qNSC1, qNSC2, aNSC1, aNSC2) that we had previously reported (Table S1) (Llorens-Bobadilla et al., 2015). Interestingly, principal component analysis revealed that the activation state and not the age is the dominant source of difference (Fig.3A,B). This result also confirms that there are at most only minimal batch effects between the young and the old data set. Notably, the proportion of qNSCs was much higher among NSCs from old mice than in those from young mice (Fig.3C). Interestingly, the expression of DNA repair-related genes was higher in aNSCs vs qNSCs irrespective of age (Fig.3D). To ensure that the much higher number of qNSC1 is not due to contaminating astrocytes, we additionally sequenced cortical and striatal astrocytes from old mice. We found many differentially expressed (DE) genes between astrocytes and qNSC1. Among them CD9, a marker previously shown to be higher expressed in NSCs than in astrocytes (Llorens-Bobadilla et al., 2015) (Fig.3E,F, Table S2). These data suggest that the increased number of cells within the qNSC1 cluster is not due to mis-labeling of contaminating astrocytes but to a higher number of bona-fide qNSC1 profiles in the aging brain.

To sequence a higher number of cells, we used the Chromium Single Cell 3' platform from 10x Genomics (sequenced libraries were produced in an identical manner). To this end, we profiled a GLAST+ fraction of V-SVZ cells enriched for NSCs from 2 and 22 MO mice (Fig.S6B). 1696 young and 1370 old cells passed the quality control and were used for further analysis (Table S4). 9 different clusters were identified using the Seurat package (Fig.4A). We used genes expressed specifically in each cluster to assign them as qNSCs (qNSC1, qNSC2), aNSCs (aNSC0, aNSC1, aNSC2), TAPs, NBs, oligodendrocytes (ODs) and oligodendrocyte progenitors (OPCs) according to previously published classification (Basak et al., 2018; Dulken et al., 2017; Llorens-Bobadilla et al., 2015) (Fig.4A, Table S1). Complementary to the clustering analysis by Seurat, we used Monocle 2 to assign a linear "pseudotime" ordering to the cells (excluding ODs and OPCs). This analysis confirmed the same lineage progression from qNSCs1 →qNSCs2 →aNSCs0 →aNSCs1 →aNSCs2

230 →TAPs →NBs for old and young NSCs (Fig.4B, S3A). The tSNE plot gives the
231 impression of a disconnection between qNSC1 and the rest of the continuum of
232 neurogenesis; this, however, might be an artifact of the t-SNE projection. To test this,
233 we inspected the distribution of Euclidean distances between cells within the qNSC1
234 and qNSC2 clusters and found them to be comparable to the qNSC2—aNSC0
235 distances but substantially lower than distances between distantly related clusters like
236 qNSC1—mature ODs (Fig.S3B). As previously observed in young NSCs, lineage
237 transitions were accompanied by a continuous gradient of expression changes
238 between the different stages (Fig.S3C,D, Table S1). Altogether, comparison of young
239 and old NSCs showed that they share the same activation states and proceed along the
240 same lineage.

241 Surprisingly, only the activation state, but not the age of the cells dictated their
242 segregation to the different clusters (Fig.4C, S3A,E). To assess in more depth the
243 similarity of young and old transcriptomes, we calculated the Euclidean distance
244 distributions of cells within a window of 5 pseudotime units comparing within and
245 between cells originating from 2 and 22 MO animals. We observed similar distances
246 within and between the age groups that were much lower than between qNSC1 and
247 qNSC2 cells (Fig.4D). The same was observed for Euclidean distance distributions of
248 cells within each separate cluster as compared to cells between qNSC1 and qNSC2
249 cluster for 10x and Smart-seq2 technologies (Fig.4E, S3F). This comparison and the
250 DE analysis of age-induced changes within each activation state (Fig. S3F, Table S2),
251 strongly indicate that age induces lower changes in fewer genes, as compared to
252 changes induced by lineage transition. In addition, comparison of the average gene
253 expression of young and old NSCs, or cells within the neurogenic lineage revealed a
254 much lower number of genes showing expression changes higher than two fold than
255 for the oligodendrocyte lineage (OD and OPCs) at young and old ages (Fig.S3H).

256 While the transcriptome associated with a specific pseudotime (i.e., position in the
257 NSC continuum) does not change with age, the distribution of pseudotime assignment
258 does. In line with the higher fraction of qNSCS in the old brain (discussed above), we
259 observed an increase in pseudotime assignments to the early qNSC1 (Fig.4F). While
260 young NSCs transit smoothly from a quiescent to a primed-quiescent state that is
261 readily followed by activation, old NSCs remain in the dormant state (qNSC1) and

fewer cells enter the aNSC0 state, to become fully activated (Fig.4F). Thus the transcriptional profile of NSCs at different ages remains similar but old NSCs tend to be in a quiescent state.

**Niche inflammatory signals keep old NSCs in a quiescent state**

We therefore set out to search for niche-derived signals that could induce quiescence. To this end, we profiled different cell types residing within the V-SVZ niche including endothelial cells (ECs), microglia (Mg), NBs and NSCs using bulk RNA sequencing from 2 and 19MO mice (Fig.S6C). Differential expression analysis revealed a common enriched expression of transcripts related to inflammatory response in every cell type (Fig.5A,B, Table S2). It also showed that ECs exhibit the highest age-related changes (Fig.5A). To explore when is the onset of the inflammatory response in NSCs we also performed NSC bulk RNA sequencing from 7 MO mice, which revealed that inflammatory genes expression at 7MO is already higher than in 2MO mice (Fig.5C).

While inflammatory genes expression was captured with bulk RNA sequencing, the observed age-imposed transcriptional changes were mild to be reliably detected at the single cell level. Overall, the differences seen in bulk sequencing data are also partly visible in the single cell SmartSeq2 data for those genes that could be detected in a sufficiently large fraction of the cells (Fig.S3G). Indeed, analysis of the read counts in single NSCs sequenced by either 10x 3' Chromium or Smart-seq2 technology, revealed that the inflammation signal is too weak and can only be detected by Smart-seq2 (in only few cells) but not by the 10x technology (Fig.S3I, Table S2). Of note, basal expression of interferon response genes is already observed in young mice, which is suggestive of a role of interferons in NSC homeostasis. We next assessed the expression of the nuclear pro-inflammatory cytokine IL33, which has been reported to activate the innate immune response by inducing interferon production in the NSC compartment of 2 and 22 MO TLX-CreER$^{T2}$YFP mice. The proportion of IL33+ NSCs changed from around 0.5% in the young V-SVZ to 15% in the old V-SVZ (Fig.5D,E). However, the NSC fraction that is retained in a quiescent state is much higher. Thus, we hypothesized that inflammatory cytokines derived from neighboring cells might contribute to induction of quiescence in the NSC compartment. Along this line, previous studies have shown that sustained inflammation activates Mg to reduce

proliferation of neighboring NSCs in the young V-SVZ (Solano Fonseca et al., 2016). In addition, ECs already induce quiescence of NSCs in a non-inflammatory state (Ottone et al., 2014). Accordingly, exposure of NSCs to inflammatory interferons (IFNα/β) greatly reduced proliferation of NSCs *in vitro* (Fig.5F). To address the contribution of interferons to the age-dependent induction of quiescence, we examined the fraction of aNSCs among adult-LRCs in 2 and 22 MO IFNα/γ receptor-knockout mice (IFNAGRKO) (Fig.S5A). We hypothesized that if inflammation, specifically interferons, are a main quiescence driver, their absence would result in NSC dynamics resembling the "no aging" scenario of our MM (Fig.1E). Consistent with the prediction of our "no aging" model, the fraction of aNSCs among LRCs did not change across time and was therefore significantly higher in old interferon-deficient animals than in old wild-type counterparts (Fig.5G). Thus, neutralizing inflammation levels off the age-related decline in activation of V-SVZ NSCs at old ages.

Finally, we investigated whether an acute inflammation inhibition in the old V-SVZ niche could activate NSCs in the old brain. Previous reports had shown that the sole neutralization of the inflammatory cytokine CXCL10 greatly improves hippocampal synaptic plasticity in the context of an interferon response triggered by a viral infection (Blank et al., 2016). Therefore, we decided to treat aged animals with a neutralizing antibody against CXCL10. Mini-osmotic pumps containing anti-CXCL10 or isotype control antibodies were implanted in the lateral ventricles of 22 MO mice and BrdU was administered for 3 days. Olfactory bulb neurogenesis was assessed by quantification of newborn NBs 4 days later (Fig.S5C). Notably, inhibition of CXCL10 significantly increased the number of NBs (Fig.5H). To confirm that this increase was due to activation of qNSCs, we administered BrdU in the drinking water for 14 days followed by a chase time of 28 days. Mini-osmotic pumps with anti-CXCL10 or isotype control antibodies were implanted 7 days before sacrificing the animals (Fig.S5A). CXCL10 neutralization significantly decreased the number of LRCs compared to IgG-treated mice indicating activation of qNSCs (Fig.5I). Thus, inhibition of CXCL10 decreased the number of qNSCs, and increased the production of NBs during homeostasis providing a causal link between inflammation and induction of quiescence in the aged brain.

**A Markov chain approach identifies the Wnt antagonist sFRP5 as an additional niche signal maintaining quiescence**

To identify additional age-related signals contributing to induction of NSC quiescence emanating from the niche we developed a Markov Chain-based computational approach (MCCM; Data S2). This approach aims at unveiling NSC-intrinsic signaling intermediates that are likely to maintain a specific cell state dictated by niche signals via a sustained effect on the downstream gene regulatory network (Ravichandran and Del Sol, 2017) (Fig.6A, Data S2). For this analysis, we used the Smart-seq2 single cell expression data of qNSCs and aNSCs from young and old mice. This approach enabled identification of key signaling intermediates likely to be constantly active or inactive in a majority of cells in the respective cellular subpopulations, among them *Bmpr1a,* a regulator of NSC quiescence (Mira et al., 2010) (Table S3). We focused on intermediates identified as uniquely active in old NSCs. The method identified eight genes uniquely expressed in old qNSC1 (Table S3). From these we focused on *Sfrp5*, a known antagonist of the Wnt signaling pathway that was strongly expressed in old qNSCs (Fig.S4A,B; TableS3). To address potential age-dependent changes in canonical Wnt-activity, we used TCF/Lef-H2B-GFP reporter mice that express an H2B-GFP fusion protein under the control of 6 TCF/Lef binding sites (Ferrer-Vaquer et al., 2010). We observed a higher fraction of GFP+NSCs among NSCs in the dorsal domain as compared to the latero-ventral domain of V-SVZ (Fig.6B-D), in line with the previously described function of Wnt-canonical signaling in generation of oligodendrocyte lineage within the dorsal domain (Ortega et al., 2013). Ependymal cells, which lie along the entire wall of the lateral ventricles, were GFP positive (Fig.6C). Importantly, the total number of GFP+NSCs significantly increased (1.4 fold) at 8MO as compared to 2MO (Fig.6D). Most DCX-Ki67+ cells which can only be active NSCs or TAPs were TCF-LEF negative indicating that canonical Wnt activity is high in qNSCs (Fig.S4C,D). Then, we hypothesized that sFRP5 antagonizes non-canonical Wnt activity thereby leading to increased canonical-activity and thus quiescence in the aging brain. Thus, we tested if neutralization of sFRP5 could decrease quiescence in old NSCs by administering a neutralizing antibody against human sFRP5 *in vivo*. We confirmed that this antibody was able to recognize mouse recombinant sFRP5 *in vitro,* and able to block Wnt3a-mediated activity in a TOPFLASH assay (Fig.S4E). Thereafter, we used the LRC protocol followed by a chase time of 6 weeks and implanted mini-osmotic pumps

containing anti-sFRP5 or isotype control antibodies 7 days before sacrificing the animals (Fig.S5A). We observed a significantly decreased number of LRCs following sFRP5 inhibition as compared to IgG-treated control old mice (Fig.6E). We thereafter tested the effect of sFRP5 inhibition in NSC-mediated repair of the injured niche. To this end we challenged the animals with TMZ and implanted mini-osmotic pumps 6 days before sacrificing them (Fig.S5B). sFRP5 inhibition significantly increased the number of proliferating cells, as assessed by a 2h-BrdU labeling protocol, in old mice as compared to IgG-treated control old mice (Fig.6F). Thus, neutralization of sFRP5 can release the brake on NSC activation in the old brain during homeostasis but also following injury.

## Discussion

### A role of quiescence in preserving a reservoir of stem cells in the aged brain

Although previous studies had already reported a shrinkage of the V-SVZ NSC pool with age (Ahlenius et al., 2009; Obernier et al., 2018; Shook et al., 2012; Silva-Vargas et al., 2016), others have reported no age-related changes (Daynac et al., 2016). This study confirms that the pool of adult V-SVZ-NSCs exhibits an age-dependent depletion, using three independent methods: counting marker positive cells by FACS, and immunostainings of embryonically- and adult-LRCs of the young and old V-SVZ. As previously hypothesized (Obernier et al., 2018) and as confirmed by the "no-aging" scenario of our mathematical modeling, the fact that NSCs have a higher probability to differentiate than to undergo self-renewing divisions leads to a time-dependent attrition. Indeed, without an age-dependent increase in the fraction of qNSCs, NSCs would undergo full depletion in the old brain. This prediction does not exclude an additional contribution of changes in other parameters but reveals that changes in "time-in-quiescence" is the only parameter which regulation allows reproducing the data on its own. Furthermore, allowing time dependent changes in quiescence and self-renewal, revealed that even if the two parameters undergo age-dependent changes, it is the time-increasing quiescence (decreasing rate of activation from quiescence), which is the major component of the regulatory process and allows explaining the observed dynamics. Notably, models accounting for other transitions, such as asymmetric divisions of the form aNSC→progenitor+qNSC, or assuming co-existence of both types of divisions, additional cell death or direct fate transitions into astrocytes (Ziebell et al., 2018), yield the same conclusion, which indicates the

393 universality of aging-induced quiescence. Accordingly, a lower fraction of LRCs that
394 become reactivated in the aging brain has been independently detected through
395 ultrastructural analysis of V-SVZ NSC following incorporation of radioactive
396 thymidine (Capilla-Gonzalez et al., 2014).

397 Contrary to the present study, others have reported an age-dependent increase of cell
398 cycle length (Daynac et al., 2016). Daynac et al., detected a higher fraction of cells
399 claimed to be in G1 state in the aging brain using FUCCI-reporter mice.
400 Unfortunately, this reporter line cannot distinguish between G1 or G0 and thus, the
401 data could be interpreted as increased cell cycle length (of G1) as done by the authors
402 or as an increased number of cells in a quiescent state (G0). In summary, our study
403 reveals that upon aging a higher fraction of NSCs is found in quiescence and this is a
404 compensatory mechanism to avoid full depletion of the NSC compartment.

405 In addition, and as opposed to the concept of malfunctioning aged stem cells, our
406 study reveals that once activated old NSCs perform as well as younger counterparts in
407 undergoing several rounds of division and generating clones with similar numbers of
408 neurons. This is also demonstrated by similar levels of DNA damage in young and old
409 NSCs, in contrary to the higher levels reported in HSCs following chronic
410 inflammation (Walter et al., 2015). Likewise, analysis of single cell and bulk
411 transcriptomes of old and young NSCs reveals that the large scale transcriptional
412 activity of the cells is given by their metabolic state and that age induces milder
413 transcriptional changes that suffice to block transition from a quiescence to an active
414 state. This study suggests that age globally changes the neurogenic niche, which
415 impairs NSC activation. Once NSCs become activated they function as well as young
416 NSCs.

417 **Inflammatory signals from the niche impose quiescence**

418 The fraction of qNSCs in the old brain is not only increased, but is also more resistant
419 to exiting quiescence even if forced by injury. Resistance to become activated has
420 been shown only *in vitro* so far and it was linked to defects in lysosomal clearance in
421 old NSCs (Leeman et al., 2018). We, however, found a link of quiescence to
422 inflammation. Inhibition of the interferon response through deletion of interferon
423 receptor $\alpha$ and $\gamma$ led to a similar fraction of aNSCs in young and old V-SVZ.

Importantly, these kinetics of the fraction of aNSCs in young and old interferon receptor deficient mice was predicted by the "no-aging" scenario.

We have previously found that activation of interferon-γ response is required to increase activation of young NSCs upon injury (Llorens-Bobadilla et al., 2015). The opposing function of interferon γ in injured young NSCs might be due to the duration of exposure to interferon, acute for injury vs. chronic exposure in aging, or to the prevalence of interferon-α/β activity in aging vs. interferon-γ in injury. Interferons derived from the choroid plexus had been reported to negatively impact adult hippocampal neurogenesis in the old brain (Baruch et al., 2014). However, how interferons decrease de-novo generation of neurons was not addressed.

Our study underlines the importance of the niche for induction of quiescence. An age-dependent expression of transcripts related to inflammatory response is globally detected in the old niche, suggestive of a major contribution of the niche in induction of NSCs quiescence. Accordingly, models of heterochronic parabiosis have identified an age-related increase of systemic inflammatory factors, such as the cytokine CCL11, which are detrimental for hippocampal neurogenesis and cognitive functions (Villeda et al., 2011). Similarly, GDF11 was identified as a systemic factor that "rejuvenates" the aged V-SVZ (Katsimpardi et al., 2014). It would be interesting to address if the rejuvenating effect by this systemic factors is solely due to inhibition of quiescence. Interestingly, increased interferon response was also detected in human aging brains (Baruch et al., 2014). In summary, our study establishes a causal link between inflammation and quiescence, and shows that an early gain of quiescence would decrease the fraction of aNSCs at young age that then would be maintained at old ages. In addition, an acute inhibition of inflammation at old age can help increasing de novo neuronal production in the old brain. Along this line, the difficulties in finding newborn neurons in the adult human brain (Kempermann et al., 2018) might be explained by the increased quiescence of adult human stem cells.

**Control of Wnt activity by the niche through sFRP5**

Finally, application of a Markov chain-based computational approach that aimed at discovering niche signals maintaining old NSCs in quiescent state, identified the Wnt antagonist sFRP5. Modulation of two other Wnt antagonists, DKK1 and sFRP3, had been reported to control expansion of hippocampal NSCs in the young and old brain

(Jang et al., 2013; Seib et al., 2013). Notably, our mathematical modeling of NSC dynamics in the hippocampus predicted that neutralization of DKK1 increases the generation of neurons in the aging brain by increasing the time in quiescence (Ziebell et al., 2018). Importantly, DKK1 antagonizes canonical Wnt signaling, as opposed to sFRP5 that putatively antagonizes non-canonical Wnt signaling, which suggest that in both neurogenic niches the switch from canonical to non-canonical is required to enter the activation state. Zhu et al. detected decreased canonical Wnt activity in the old V-SVZ as compared to younger counterparts (Zhu et al., 2014). This study used an Axin2-βGal reporter as read out for canonical Wnt signal and did not specifically address its expression in NSCs but in the whole V-SVZ tissue, which as we show now is masked by the highest expression in the ependymal compartment. Using a TCF/Lef reporter, we found that canonical Wnt activity was majorly found in Ki67 negative cells, and thus, qNSCs. We hypothesize that a switch to non-canonical Wnt activity is required to enter activation at all ages, but in the aging V-SVZ this activity can be inhibited by sFRP5. Accordingly, we show that an acute block of sFRP5 increased the fraction of actively cycling NSCs in the old brain following homeostasis and a temozolomide-injury. Likewise, inhibition of canonical Wnt activity in the old bone improved bone healing (Baht et al., 2015). In the hematopoietic system, however, a detrimental increase of non-canonical Wnt signaling was found in aged HSCs (Florian et al., 2013). In summary, Wnt activity, either canonical or non-canonical, crucially regulates activation of adult somatic stem cells. Importantly, a link between Wnt activity and inflammation has been speculated in the old and the injured brain (Marchetti and Pluchino, 2013). A good example are Mg that use non-canonical or canonical Wnt activity to respectively activate or inhibit expression of inflammatory cytokines (Marchetti and Pluchino, 2013). Also, inflamed Mg decrease NSC proliferation and neuronal production (Solano Fonseca et al., 2016). Thus, we speculate that an attempt to block inflammation in niche cells such as Mg, through increased expression of antagonist of the non-canonical Wnt signaling results in a brake on activation of NSCs. This would explain why blocking inflammation or expression of sFRP5 would similarly lead to increased exit of quiescence in old NSCs.

In summary, this study reveals that quiescence induction is used to preserve a small pool of NSCs in the old brain. Aged NSCs perform as well as their younger

counterparts once activated but are more resistant to becoming activated. Analysis of the bulk or individual transcriptomes of NSCs shows that transitions throughout the different activation states are underlined by profound transcriptional changes in metabolism-related programs that can be readily detected at the single cell level. However, age-related transcriptional changes are too mild to be reliably detected at the single cell level and could only be detected by bulk-sequencing or predicted by the Markov chain approach. In addition, this study reveals a causal link between maintenance of quiescence, inflammation and non-canonical Wnt-activity. Understanding how to modulate the balance between quiescence and activation of NSCs in the old brain will be critical to preserve stem cell function in the aging brain.

**Author contributions**

Acquisition, analysis and interpretation of experimental data: G.K.; Bioinformatic analysis of sc RNAseq: S.A., D.B., S.Z.; Mathematical model of NSC dynamics: A.M-C., F.Z., T.S.; Markov chain based computation approach: R.S., A.dS.M; Acquisition of cell counts used in the MM: F.C.M., J.K.; Assistance in animal experiments: S.L.; involved in inflammation-related data: J.B.; Smart-seq2 RNAseq of young NSCs: E.LL-B.; Single Cell 3' platform libraries: B.K., M.J.P.; Time lapse lineage tracing: B.Be., W.Q.; Top Flash assay: B. Bi.; CXCL10 antibody: C.U.; Comet assay: S.P.; Supervision: A.M.-V., A.M.C., S.A., A.dS.M., B.Be.; Writing and editing: A.M.-V., G.K., A.M.C., S.A., A.dS., B.Be.; Project conceptualization: A.M.-V., G.K.; Project design and oversight: A.M.-V.

**Acknowledgements**

We thank S. Wolf from the DKFZ Genomics and Proteomics Core Facility; V. Eckstein from the Heidelberg Universty Hospital FACS Core Facility; Monika Langlotz from the ZMBH FACS Core Facility, Reinhard Gliniorz for technical assistance in performing the comet assay; Gonzalo Saiz-Castro and Klara Zwadlo for technical assistance; Hai-Kun Liu for Tlx-CreER$^{T2}$ mice; Mathias Heikenwälder for TCF/Lef reporter mice; The Light Microscopy Core Facility for support; This work was supported by the DFG (SFB873, SFB1324, SFB1036, INST 161/875-2), the Helmholtz Alliance for aging and metabolic programming (AMPro) and the DKFZ. W.F. is supported by the "China scholarship council)".

**Declaration of Interests**

The authors declare no competing interests.

## References


Ahlenius, H., Visan, V., Kokaia, M., Lindvall, O., and Kokaia, Z. (2009). Neural Stem and Progenitor Cells Retain Their Potential for Proliferation and Differentiation into Functional Neurons Despite Lower Number in Aged Brain. Journal of Neuroscience 29, 4408–4419.

Baht, G.S., Silkstone, D., Vi, L., Nadesan, P., Amani, Y., Whetstone, H.C., Wei, Q., and Alman, B.A. (2015). Exposure to a youthful circulaton rejuvenates bone repair through modulation of β-catenin. Nature Communications 6, 501.

Baruch, K., Deczkowska, A., David, E., Castellano, J.M., Miller, O., Kertser, A., Berkutzki, T., Barnett-Itzhaki, Z., Bezalel, D., Wyss-Coray, T., et al. (2014). Aging-induced type I interferon response at the choroid plexus negatively affects brain function. Science 346, 89–93.

Basak, O., Krieger, T.G., Muraro, M.J., Wiebrands, K., Stange, D.E., Frias-Aldeguer, J., Rivron, N.C., van de Wetering, M., van Es, J.H., van Oudenaarden, A., et al. (2018). Troy+ brain stem cells cycle through quiescence and regulate their number by sensing niche occupancy. Proc. Natl. Acad. Sci. U.S.a. 201715911.

Berger, B.S., Acebron, S.P., Herbst, J., Koch, S., and Niehrs, C. (2017). Parkinson's disease- associated receptor GPR37 is an ER chaperone for LRP6. EMBO Rep. 18, 712–725.

Blank, T., Detje, C.N., Spieß, A., Hagemeyer, N., Brendecke, S.M., Wolfart, J., Staszewski, O., Zöller, T., Papageorgiou, I., Schneider, J., et al. (2016). Brain Endothelial- and Epithelial-Specific Interferon Receptor Chain 1 Drives Virus-Induced Sickness Behavior and Cognitive Impairment. Immunity 44, 901–912.

Breuer, K., Foroushani, A.K., Laird, M.R., Chen, C., Sribnaia, A., Lo, R., Winsor, G.L., Hancock, R.E.W., Brinkman, F.S.L., and Lynn, D.J. (2013). InnateDB: systems biology of innate immunity and beyond--recent updates and continuing curation. Nucleic Acids Res. 41, D1228–D1233.

Burnham, K. P., and Anderson, D. R. (2002) Model selection and multimodel inference: A practical information-theoretic approach. Springer.

Calzolari, F., Michel, J., Baumgart, E. V., Theis, F., Gotz, M., and Ninkovic, J. (2015). Fast clonal expansion and limited neural stem cell self-renewal in the adult subependymal zone. Nat. Neurosci. 18, 490–492.

Capilla-Gonzalez, V., Cebrian-Silla, A., Guerrero-Cazares, H., Garcia-Verdugo, J.M., and Quiñones-Hinojosa, A. (2014). Age-related changes in astrocytic and ependymal cells of the subventricular zone. Glia 62, 790–803.

Daynac, M., Morizur, L., Chicheportiche, A., Mouthon, M.-A., and Boussin, F.D. (2016). Age-related neurogenesis decline in the subventricular zone is associated with specific cell cycle regulation changes in activated neural stem cells. Sci. Rep. 6, 21505.

561 Dobin, A., Davis, C.A., Schlesinger, F., Drenkow, J., Zaleski, C., Jha, S., Batut, P.,
562 Chaisson, M., and Gingeras, T.R. (2013). STAR: ultrafast universal RNA-seq aligner.
563 Bioinformatics 29, 15–21.

564 Dulken, B.W., Leeman, D.S., Boutet, S.C., Hebestreit, K., and Brunet, A. (2017).
565 Single-Cell Transcriptomic Analysis Defines Heterogeneity and Transcriptional
566 Dynamics in the Adult Neural Stem Cell Lineage. Cell Rep 18, 777–790.

567 Ernst, A., Alkass, K., Bernard, S., Salehpour, M., Perl, S., Tisdale, J., Possnert, G.,
568 Druid, H., and Frisén, J. (2014). Neurogenesis in the Striatum of the Adult Human
569 Brain. Cell 156, 1072–1083.

570 Ferrer-Vaquer, A., Piliszek, A., Tian, G., Aho, R.J., Dufort, D., and Hadjantonakis,
571 A.-K. (2010). A sensitive and bright single-cell resolution live imaging reporter of
572 Wnt/ß-catenin signaling in the mouse. BMC Dev. Biol. 10, 121.

573 Florian, M.C., Nattamai, K.J., Dörr, K., Marka, G., Überle, B., Vas, V., Eckl, C.,
574 Andrä, I., Schiemann, M., Oostendorp, R.A.J., et al. (2013). A canonical to non-
575 canonical Wnt signalling switch in haematopoietic stem-cell ageing. Nature 503, 392–
576 396.

577 Fuentealba, L.C., Rompani, S.B., Parraguez, J.I., Obernier, K., Romero, R., Cepko,
578 C.L., and Alvarez-Buylla, A. (2015). Embryonic Origin of Postnatal Neural Stem
579 Cells. Cell 161, 1644–1655.

580 Haas, B.J., Papanicolaou, A., Yassour, M., Grabherr, M., Blood, P.D., Bowden, J.,
581 Couger, M.B., Eccles, D., Li, B., Lieber, M., et al. (2013). De novo transcript
582 sequence reconstruction from RNA-seq using the Trinity platform for reference
583 generation and analysis. Nature Protocols 8, 1494–1512.

584 Hilsenbeck, O., Schwarzfischer, M., Skylaki, S., Schauberger, B., Hoppe, P.S.,
585 Loeffler, D., Kokkaliaris, K.D., Hastreiter, S., Skylaki, E., Filipczyk, A., et al. (2016).
586 Software tools for single-cell tracking and quantification of cellular and molecular
587 properties. Nature Biotechnology 34, 703.

588 Huang, S., Hendriks, W., Althage, A., Hemmi, S., Bluethmann, H., Kamijo, R.,
589 Vilcek, J., Zinkernagel, R., and Aguet, M. (1993). Immune response in mice that lack
590 the interferon-gamma receptor. Science 259, 1742–1745.

591 Jacquet, B.V., Salinas-Mondragon, R., Liang, H., Therit, B., Buie, J.D., Dykstra, M.,
592 Campbell, K., Ostrowski, L.E., Brody, S.L., and Ghashghaei, H.T. (2009). FoxJ1-
593 dependent gene expression is required for differentiation of radial glia into ependymal
594 cells and a subset of astrocytes in the postnatal brain. Development 136, 4021–4031.

595 Jang, M.-H., Bonaguidi, M.A., Kitabatake, Y., Sun, J., Song, J., Kang, E., Jun, H.,
596 Zhong, C., Su, Y., Guo, J.U., et al. (2013). Secreted frizzled-related protein 3
597 regulates activity-dependent adult hippocampal neurogenesis. Cell Stem Cell 12, 215–
598 223.

599 Katsimpardi, L., Litterman, N.K., Schein, P.A., Miller, C.M., Loffredo, F.S.,
600 Wojtkiewicz, G.R., Chen, J.W., Lee, R.T., Wagers, A.J., and Rubin, L.L. (2014).

601 Vascular and Neurogenic Rejuvenation of the Aging Mouse Brain by Young
602 Systemic Factors. Science 344, 630–634.

603 Kempermann, G., Gage, F.H., Aigner, L., Song, H., Curtis, M.A., Thuret, S., Kuhn,
604 H.G., Jessberger, S., Frankland, P.W., Cameron, H.A., et al. (2018). Human Adult
605 Neurogenesis: Evidence and Remaining Questions. Cell Stem Cell 23, 25–30.

606 Kong, Y. (2011). Btrim: a fast, lightweight adapter and quality trimming program for
607 next-generation sequencing technologies. Genomics 98, 152–153.

608 Leeman, D.S., Hebestreit, K., Ruetz, T., Webb, A.E., McKay, A., Pollina, E.A.,
609 Dulken, B.W., Zhao, X., Yeo, R.W., Ho, T.T., et al. (2018). Lysosome activation
610 clears aggregates and enhances quiescent neural stem cell activation during aging.
611 Science 359, 1277–1283.

612 Lim, D. A., and Alvarez-Buylla, A. (2016). The adult ventricular-subventricular zone
613 (v-svz) and olfactory bulb (ob) neurogenesis. Cold Spring Harbor Perspectives in
614 Biology 8, a018820.

615 Liu, H.K., Wang, Y., Belz, T., Bock, D., Takacs, A., Radlwimmer, B., Barbus, S.,
616 Reifenberger, G., Lichter, P., and Schutz, G. (2010). The nuclear receptor tailless
617 induces long-term neural stem cell expansion and brain tumor initiation. Genes &
618 Development 24, 683–695.

619 Liu, Y., Beyer, A., and Aebersold, R. (2016). On the Dependency of Cellular Protein
620 Levels on mRNA Abundance. Cell 165, 535-550.

621 Llorens-Bobadilla, E., Zhao, S., Baser, A., Saiz-Castro, G., Zwadlo, K., and Martin-
622 Villalba, A. (2015). Single-Cell Transcriptomics Reveals a Population of Dormant
623 Neural Stem Cells that Become Activated upon Brain Injury. Cell Stem Cell 17, 329–
624 340.

625 Marchetti, B., and Pluchino, S. (2013). Wnt your brain be inflamed? Yes, it Wnt!
626 Trends Mol Med 19, 144–156.

627 Mich, J.K., Signer, R.A., Nakada, D., Pineda, A., Burgess, R.J., Vue, T.Y., Johnson,
628 J.E., and Morrison, S.J. (2014). Prospective identification of functionally distinct stem
629 cells and neurosphere-initiating cells in adult mouse forebrain. eLife 3, e02669.

630 Mira, H., Andreu, Z., Suh, H., Lie, D.C., Jessberger, S., Consiglio, A., San Emeterio,
631 J., Hortigüela, R., Marqués-Torrejón, M.Á., Nakashima, K., et al. (2010). Signaling
632 through BMPR-IA Regulates Quiescence and Long-Term Activity of Neural Stem
633 Cells in the Adult Hippocampus. Cell Stem Cell 7, 78–89.

634 Muller, U., Steinhoff, U., Reis, L., Hemmi, S., Pavlovic, J., Zinkernagel, R., and
635 Aguet, M. (1994). Functional role of type I and type II interferons in antiviral defense.
636 Science 264, 1918–1921.

637 Obernier, K., Cebrian-Silla, A., Thomson, M., Parraguez, J.I., Anderson, R., Guinto,
638 C., Rodas Rodriguez, J., Garcia-Verdugo, J.M., and Alvarez-Buylla, A. (2018). Adult
639 Neurogenesis Is Sustained by Symmetric Self-Renewal and Differentiation. Cell Stem
640 Cell 22, 221–234.e228.

641 Oh, J., Lee, Y.D., and Wagers, A.J. (2014). Stem cell aging: mechanisms, regulators
642 and therapeutic opportunities. Nature Publishing Group 20, 870–880.

643 Ortega, F., Gascón, S., Masserdotti, G., Deshpande, A., Simon, C., Fischer, J., Dimou,
644 L., Lie, D.C., Schroeder, T., and Berninger, B. (2013). Oligodendrogliogenic and
645 neurogenic adultsubependymal zone neural stem cells constitutedistinct lineages and
646 exhibit differential responsivenessto Wnt signalling. Nature Cell Biology 15, 602–
647 613.

648 Ottone, C., Krusche, B., Whitby, A., Clements, M., Quadrato, G., Pitulescu, M.E.,
649 Adams, R.H., and Parrinello, S. (2014). Direct cell–cell contact with the vascular
650 niche maintains quiescent neural stem cells. Nature Cell Biology 16, 1045–1056.

651 Picelli, S., Faridani, O.R., Björklund, A.K., Winberg, G., Sagasser, S., and Sandberg,
652 R. (2014). Full-length RNA-seq from single cells using Smart-seq2. Nature Protocols
653 9, 171–181.

654 Ponti, G., Obernier, K., Guinto, C., Jose, L. , Bonfanti, L., and Alvarez-Buylla, A.
655 (2013). Cell cycle and lineage progression of neural progenitors in the ventricular-
656 subventricular zones of adult mice. PNAS 110, E1045–E1054.

657 Qiu, X., Mao, Q., Tang, Y., Wang, L., Chawla, R., Pliner, H.A., and Trapnell, C.
658 (2017). Reversed graph embedding resolves complex single-cell trajectories. Nature
659 Methods 14, 979–982.

660 Ravichandran, S., and Del Sol, A. (2017). Identifying niche-mediated regulatory
661 factors of stem cell phenotypic state: a systems biology approach. FEBS letters 591,
662 560-569.

663 Rezza, A., Sennett, R., and Rendl, M. (2014). Adult stem cell niches: cellular and
664 molecular components. Current topics in developmental biology 107, 333-372.

665 Rieger, M.A., Hoppe, P.S., Smejkal, B.M., Eitelhuber, A.C., and Schroeder, T.
666 (2009). Hematopoietic Cytokines Can Instruct Lineage Choice. Science 325, 217–
667 218.

668 Robinson, M.D., and Oshlack, A. (2010). A scaling normalization method for
669 differential expression analysis of RNA-seq data. Genome Biol. 11, R25.

670 Seib, D.R.M., Corsini, N.S., Ellwanger, K., Plaas, C., Mateos, A., Pitzer, C., Niehrs,
671 C., Celikel, T., and Martin-Villalba, A. (2013). Loss of Dickkopf-1 restores
672 neurogenesis in old age and counteracts cognitive decline. Cell Stem Cell 12, 204–
673 214.

674 Shalek, A.K., Satija, R., Adiconis, X., Gertner, R.S., Gaublomme, J.T.,
675 Raychowdhury, R., Schwartz, S., Yosef, N., Malboeuf, C., Lu, D., et al. (2013).
676 Single-cell transcriptomics reveals bimodality in expression and splicing in immune
677 cells. Nature 498, 236–240.

678 Shalek, A.K., Satija, R., Shuga, J., Trombetta, J.J., Gennert, D., Lu, D., Chen, P.,
679 Gertner, R.S., Gaublomme, J.T., Yosef, N., et al. (2014). Single-cell RNA-seq reveals
680 dynamic paracrine control of cellular variation. Nature 510, 363–369.

Shi, Z., Geng, Y., Liu, J., Zhang, H., Zhou, L., Lin, Q., Yu, J., Zhang, K., Liu, J., Gao, X., et al. (2017). Single-cell transcriptomics reveals gene signatures and alterations associated with aging in distinct neural stem/progenitor cell subpopulations. Protein Cell 7, 744.

Shook, B.A., Manz, D.H., Peters, J.J., Kang, S., and Conover, J.C. (2012). Spatiotemporal Changes to the Subventricular Zone Stem Cell Pool through Aging. Journal of Neuroscience 32, 6947–6956.

Silva-Vargas, V., Maldonado-Soto, A.R., Mizrak, D., Codega, P., and Doetsch, F. (2016). Age-Dependent Niche Signals from the Choroid Plexus Regulate Adult Neural Stem Cells. Cell Stem Cell 19, 643–652.

Solano Fonseca, R., Mahesula, S., Apple, D., Raghunathan, R., Dugan, A., Cardona, A., O'Connor, J., and Kokovay, E. (2016). Neurogenic niche microglia undergo positional remodeling and progressive activation contributing to age-associated reductions in neurogenesis. Stem Cells and Development scd.2015.0319.

Stewart, W.J. (1994). An Introduction to the Numerical Solution of Markov Chains (New Jersey: Princeton University Press).

Stiehl, T., and Marciniak-Czochra, A. (2011). Characterization of stem cells using mathematical models of multistage cell lineages, Math.Comp. Models 53, 1505–1517.

Villeda, S.A., Luo, J., Mosher, K.I., Zou, B., Britschgi, M., Bieri, G., Stan, T.M., Fainberg, N., Ding, Z., Eggel, A., et al. (2011). The ageing systemic milieu negatively regulatesneurogenesis and cognitive function. Nature 477, 90–94.

Walter, D., Lier, A., Geiselhart, A., Thalheimer, F.B., Huntscha, S., Sobotta, M.C., Moehrle, B., Brocks, D., Bayindir, I., Kaschutnig, P., et al. (2015). Exit from dormancy provokes DNA-damage-induced attrition in haematopoietic stem cells. Nature 520, 549–552.

Yu, G., Wang, L.-G., Han, Y., and He, Q.-Y. (2012). clusterProfiler: an R Package for Comparing Biological Themes Among Gene Clusters. OMICS: a Journal of Integrative Biology 16, 284–287.

Zhu, Y., Demidov, O.N., Goh, A.M., Virshup, D.M., Lane, D.P., and Bulavin, D.V. (2014). Phosphatase WIP1 regulates adult neurogenesis and WNT signaling during aging. J. Clin. Invest. 124, 3263–3273.

Ziebell, F., Dehler, S., Martin-Villalba, A., and Marciniak-Czochra, A. (2018). Revealing age-related changes of adult hippocampal neurogenesis using mathematical models. Development 145, dev153544.

Ziebell, F., Martin-Villalba, A., and Marciniak-Czochra, A. (2014). Mathematical modelling of adult hippocampal neurogenesis: effects of altered stem cell dynamics on cell counts and bromodeoxyuridine-labelled cells. Journal of the Royal Society Interface 11, 20140144.

**Figure Legends**

**Figure 1, A time-dependent increase in quiescence maintains a stem cell reservoir at old age.** A) FACS analysis of total number of NSCs, qNSCs, aNSCs and TAPs from both V-SVZs of mice of different ages (2 MO, n=6 replicates of 2 pooled mice; 7 MO, n=3 replicates of 2 pooled mice; 22 MO, n=3 pools of 3 mice; bar and whiskers denote mean ± SD; Tukey-Kramer multiple-comparisons test). B) Representative pictures of 2 MO and 14 MO SVZ (scale bar: 20 μm; white arrows indicate E-LRCs). C) Quantification of total number of YFP+Sox2+BrdU+DCX-S100b- cells/SVZ/Section at 2 and 14 MO (n=3 mice/group; bar and whiskers denote mean ± SD; Student's t-test). D) Schematic representation of MM. qNSCs can enter the cell cycle to become aNSCs. aNSCs divide to either produce two qNSCs or two TAPs (progn). Progenitors have the capacity of n symmetric self-renewing divisions, which give rise to neuroblasts (nblast). Fit of neurogenesis model to the data assuming no aging (E); cell cycle lengthening (F); increasing self-renewal (G); or increasing quiescence (H) (red represents model and black experimental data). I) Quantification of fraction of Ki67+ among YFP+Sox2+BrdU+S100b- cells at 2, 7 and 14 MO (n=3 mice/group; bar and whiskers denote mean ± SD; Tukey-Kramer multiple-comparisons test). *p <0.05; ** p <0.01; *** p <0.001; n.s.: not significant.

**Figure 2, qNSCs are resistant to activation while aNSCs exhibit similar behavior in the young and old brain.** A) Schematic representation of experimental setup. B) Quantification of BrdU+ cells/SVZ/Section in 2 MO and 22 MO mice (Each data point represents a mouse; bar and whiskers denote mean ± SD; Tukey-Kramer multiple-comparisons test; statistics compared to the control group –saline-). C) Phase contrast time-lapse microscopy pictures of sorted 2 MO and 22 MO aNSCs for 5 days. (day:hour:minute). Post-imaging immunocytochemistry for GFAP (white), NG2 (red) and βIII-tubulin (green) and lineage tree for the depicted clones (scale bar: 20 μm). D) Average clone size of dividing cells. E) Average number of division rounds per clone. F) Average cell cycle length per clone (2 MO n=39 clones, 22 MO n=21 clones; bar and whiskers denote mean ±SEM). *** p <0.001; n.s.: not significant.

**Figure 3, The individual transcriptomes of young and old NSCs (Smart-seq2 technology) show an increased fraction of old qNSCs** A) PCA plot for the transcriptomes of 92 NSCs of 2 MO mice (circles) from Llorens-Bobadilla et al., 2015 and 133 NSCs of 23 MO mice (triangles). Colors indicate different activation states, as identified from the hierarchical clustering in Llorens-Bobadilla et al., 2015. See Table S1. B) PCA plots of individual subpopulations of NSCs sequenced with the

Smart-seq2 protocol. Green dots represent cells from 2 MO and purple triangles cells from 23 MO mice. C) Pie charts representing the fraction of NSCs in different activation states from 2 and 23 MO mice. D) Heatmap of manually selected genes involved in DNA damage response pathways. E) Log2-transformed TPM gene expression values of all the DE genes (with absolute log fold change >1 and $p<0.01$) between old qNSC1 and astrocytes, shown for qNSC1, qNSC2 cells and astrocytes from the Smart-seq2 data. Upper half: upregulated genes that are expressed higher in qNSC1s than in astrocytes. Lower half: downregulated genes that are expressed lower in qNSC1s than in astrocytes. See Table S2. F) Box plots of CD9 expression in astrocytes and qNSC1 cells from 2 and 23 MO mice (Likelihood ratio test, adjusted pval <0.003).

**Figure 4, Single cell transcriptomics (Chromium Cell 3' platform) uncovers a remarkable similarity between young and old NSCs.** A) t-distributed stochastic neighborhood-embedding (t-SNE) of 1696 cells from 2MO and 1370 cells from 22 MO mice. Colors indicate assigned activation states and cell types. B) Ordering of young and old single cell transcriptomes using monocle 2. The pseudotime order agrees with the assigned activation states. C) Same t-SNE map as in panel A, with colours representing cells from 2 (green) and 22 MO (purple) mice. The good intermixing indicates absence of noticeable batch effects. D) Euclidean distance distributions of cells within a window of 5 pseudotime units comparing within and between cells originating from 2 and 22 MO animals. Euclidean distance between cells from qNSC1 and qNSC2 activation states within a pseudotime window of 5 units serves as reference. Lines denote the mean Euclidean distance observed. E) Comparison of Euclidean distance distributions between cells of the same activation state from young and old, young and young, old and old mice (overlayed). Euclidean distance between qNSC1 and qNSC2 serves as reference. F) Density estimate of cell number along the pseudotime from qNSC1 to aNSC2 per age group.

**Figure 5, Niche inflammatory signals keep old NSCs in a quiescent state.** A) Mean log2 fold change per gene in the comparison between 19 and 2MO bulk samples (NSCs, ECs, Mg and NB cells). Red dots represent significantly DE genes (padj<0.05, absolute log2 fold change >1). Blue dots represent significantly upregulated genes annotated as innate immune response genes by InnateDB (Breuer et al., 2013). B) Gene ontology analysis of genes upregulated upon aging (>2 fold change, pvalue<0.05) of bulk populations from different SVZ cell types. See Table

S2. C) Mean log2 fold change per gene in the comparison between 7 vs 2 MO bulk sequencing samples of NSCs. Red dots represent significantly DE genes (padj<0.05, absolute log2 fold change >1). Blue dots represent significantly upregulated genes annotated as innate immune response genes by InnateDB (Breuer et al., 2013) from the comparison of 19 vs 2 MO. D) Representative picture of old SVZ immunostainings for IL33, YFP and DCX (scale bar: 10 μm; white arrows indicate Il33- and yellow Il33+ NSCs). E) Fraction of IL33+ among YFP+SOX2+DCX- cells at 2 and 22 MO mice (n=3 mice/group; bar and whiskers denote mean ± SD; Student's t test). F) % of Ki67+ among Sox2+ NSCs after 48 hours of treatment with IFNα/β; (n=4 primary cell lines; bar and whiskers denote mean ± SD; Student's t test). G) % of Ki67+ among Sox2+LRC+DCX- NSCs in 2 MO and 22 MO WT and IFNAGR KO mice (n=3 mice/group; bar and whiskers denote mean ± SD; Tukey-Kramer multiple-comparisons test). H) Number of DCX+BrdU+ cells arriving in the OB after CXCL10 inhibition normalized to the area (IgG n=8 mice, anti-CXCL10 n=7 mice; bar and whiskers denote mean ± SD; Student's t test). I) Number of LRCs (BrdU+DCX-S100b-)/SVZ/Section after CXCL10 inhibition (n=3 mice/group; bar and whiskers denote mean ± SD; Student's t test). * p<0.05; ** p <0.01; **** p <0.0001; n.s.: not significant.

**Figure 6, A Markov chain approach identifies the Wnt antagonist sFRP5 as additional niche signals maintaining quiescence.** A) MCCM of a toy-signaling network in two different niches. The node colors in the network represent the probability of the signal to be in a specific node (molecule). The edge thickness represents the interaction probability of the two molecules inferred from single-cell RNA-seq. At t=0, all nodes have equal probability to contain the signal, and with increasing time the probability of signal to be present in a molecule changes and eventually, the system reaches a steady state probability distribution, based on which the niche specific signaling molecules (in purple) are identified. See Table S3. B, C) Representative pictures of the dorsal (B) or lateroventral (C) SVZ from 2 MO and 8 MO mice (White arrows indicate TCF/Lef+ and yellow TCF/Lef- NSCs) (scale bars; left panel: 20 μm, right panel: 10 μm). D) Quantification of TCF/Lef+ among GFAP+SOX2+DCX-S100b- NSCs in whole, dorsal and lateroventral SVZ (2 MO n=2, 8MO n=3; bar and whiskers denote mean ± SD; Student's t test). E) Number of LRCs (BrdU+DCX-) after IgG or anti-sFRP5 (n=4 mice/group; bar and whiskers

denote mean ± SD; Student's t test). F) Number of BrdU+ cells in the SVZ after TMZ-injury and treatment with IgG or anti-sFRP5 (n=10 mice/group; bar and whiskers denote mean ± SD; Student's t test). *p<0.05.

**Supplemental Figure Legends**

**Figure S1, Quiescence of NSCs increases upon aging, Related to Fig.1.** A) Representative picture of cells from the V-SVZ 2MO TLX-CreER$^{T2}$YFP (scale bar: 20 μm). B) Fraction of BrdU+ cells among YFP+DCX- cells in 2, 7 and 22 MO (Each data point represents one mouse; bar and whiskers denote mean ± SD; Tukey-Kramer multiple-comparisons test). C) Representative picture of a Ki67+LRC+ cell in the SVZ of 22 MO. (Scale bar:10 μm) D) Fraction of Ki67+ cells among LRC+DCX- in 2, 7 and 22MO (n=3 mice/group; bar and whiskers denote mean ± SD; Tukey-Kramer multiple-comparisons test). E) Fit of the neurogenesis model with increase of self-renewal during aging. The cell counts at age 0 are in the order of 10^6. F) Upper panel: Fit of the neurogenesis model with simultaneous increase of quiescence and self-renewal during aging. Lower panels: Model with simultaneous increase of quiescence and self-renewal during aging: Time course of self-renewal fraction and activation rate. The activation rate from quiescence significantly decreases in time. The self-renewal fraction only slightly changes at younger ages. The red curves correspond to model simulations. Each black dot denotes experimental data of one mouse. G) Representative pictures of embryonically BrdU-labelled YFP+ cells that are Ki67+ (yellow arrow) or Ki67- (white arrow) (scale bar: 10 μm). *p<0.05; ** p <0.01; *** p <0.001; n.s.: not significant.

**Figure S2, DNA damage does not increase upon aging and old aNSCs have similar properties to young, Related to Fig.2.** A) Maximum intensity projection micrographs (scale bar: 10 μm) of dorsal SVZ from 2 and 22 MO mice at different time points after TMZ injection. (note the increase in autofluorescent lipofuscin speckles all over the 22 MO brains). B) Representative pictures of intact or damaged nuclei after 5Gy gamma irradiation. C) Quantification of the olive tail moment (active old n=257 cells, active young n=274 cells, quiescent old n=150 cells, quiescent young n=245 cells). D) Lineage trees of 2 MO and 22 MO aNSCs. E) Representative pictures of spheres derived from single aNSCs from 2, 7 and 22 MO mice (scale bar:

200 μm). F) Quantification of sphere diameter (2 MO and 22 MO n=4, 7MO n=2; bar and whiskers denote mean ± SD; Tukey-Kramer multiple-comparisons test). n.s.: not significant.

**Figure S3, Transcriptomic analysis, Related to Fig. 3 and 4.** A) tSNE map of cells from the neurogenic lineage colored by pseudotime as assigned by monocle2 (10x 3' Chromium). B) Distributions of euclidean distances between cells from different activation states. Although there is a gap between the qNSC1 and qNSC2 in the t-SNE plot the comparison of the distance distibutions shows that the distance between qNSC1 and qNSC2 is similar to the distance of qNSC2 and aNSC0, which are not separated by a gap. The distance distribution of qNSC1 compared to OD as expected shows a higher distance between these cell types, while the aNSC clusters are closer together (10x 3' Chromium). C) Heatmap of differentially expressed genes for the identified cell clusters (gene-wise z-scores). Columns (cells) are sorted by their monocle assigned pseudotime from left to right (for cells from the neurogenic lineage), while cells from OPC and OD are added to the right without further sorting. Rows (genes) were ordered by increasing onset of expression along the pseudotime from top to bottom. Differentially expressed genes for OPC and OD were added to the bottom. See Table S1 (10x 3' Chromium). D) Heatmap displaying expression of selected genes (gene-wise z-scores) from recently published sc RNAseq data of young SVZ (Basak et al., 2018) in cells of our study sequenced with the 10x genomics platform (10x 3' Chromium). E) PCA plots of individual subpopulations of NSCs sequenced (10x 3' Chromium). F) Comparison of euclidean distance distributions between cells of the same activation state from young and old, young and young, old and old mice. Euclidean distance between qNSC1 and qNSC2 serves as reference. (Smart-seq2). The right panel shows a detailed view of changes in mean expression and SD for each gene between old and young within qNSC1 (upper) and in the transition qNSC1→qNSC2 in young and old (lower). G) Scatter plot of genes in the Smart-seq2 data that were differentially expressed upon aging in bulk NSCs. Y-axis indicates the difference of the average log-transformed TPM values between old and young. X-axis denotes the fraction of cells without any reads for this gene in either old or young. To this end we calculated the fraction separately for young and old and used the larger value. Color denotes the direction of change in the bulk sequencing

888 data. H) Scatter plots comparing gene expression between 22 and 2 MO mice,
889 averaged over all NSCs, the neurogenic lineage, ODs or OPCs. Dotted lines represent
890 2 fold-change (genes >2 FC are shown in black) (10x 3' Chromium). I) Barplots
891 representing the percentage of cells with read counts stratified in 4 different intervals
892 (0, 1-5, 5-50, >50) of top genes related to immune response upregulated in Bulk
893 sequencing between old and young NSCs in (10x 3' Chromium and Smart-seq2).

894 **Figure S4, Related to Fig. 6.** A) Expression of Sfrp5 from Smart-seq2 single cell
895 data (bar and whiskers denote mean ± SD). B) Expression of Sfrp5 in bulk
896 populations of NSCs at 2, 7 and 19 MO NSCs (dots represent biological replicates).
897 C) Representative pictures of TCF/Lef expression among Ki67+ cells (scale bars: 20
898 μm) in 2 and 8 MO mice (arrows indicate examples of Ki67+ cells that are TCF/Lef-.
899 D) Quantification of TCF/LEF+ among Ki67+ cells (2 MO n=2, 8MO n=3; data
900 shown as mean ±SD). E) TOPFLASH assay with HEK 293 cells (Data shown as
901 mean ±SD).
902
903 **Figure S5, Related to Fig. 1, 2, 5, 6, S1.** Experimental outlines of experiments
904 across the article. A) Approaches to label and follow e-LRC or LRC NSCs. B)
905 Labelling of proliferating cells in the SVZ with a 2 hr pulse of BrdU. C) Labelling of
906 newly-born NBs arriving at the olfactory bulb.
907
908 **Figure S6, Related to Fig. 1, 2, 3, 4, 5, S2.** FACS strategies followed for the
909 isolation and analysis of V-SVZ cell populations. A) Strategy for the isolation of
910 qNSCs, aNSCs and TAPs. B) Strategy for preparation of libraries for 10x Chromium
911 3'. C) Strategy followed to isolate different populations of cells from the V-SVZ
912 niche.

913 **STAR Methods**

914 **Author information**

915 RNAseq raw sequence data is available from GEO (Accession number: GSE115626).
916 All the analysis is described in the *methods* section. The complete R/Bioconductor
917 software package will available upon acceptance on the authors' webpage
918 (https://martin-villalba-lab.github.io/). Correspondence and requests for materials
919 should be addressed to AMV (a.martin-villalba@dkfz-heidelberg.de).

**Mouse strains**

Male C57BL/6 mice were purchased from Janvier or bred in house at the DKFZ Center for Preclinical Research facility. Male IFNRKO (Huang et al., 1993; Muller et al., 1994) (IFNAR-/-IFNGR-/-) 2 and 22 MO were backcrossed to a C57BL6 background. Male and female Tlx-CreER$^{T2}$YFP (Liu et al., 2010) were used according to the protocols in Figure S5. Male 2 MO and 8 MO TCF/Lef:H2B/GFP were used to assess TCF/Lef activity (Ferrer-Vaquer et al., 2010). Animals had *ad libitum* access to food and water and were kept under a 12hr light-12hr dark cycle. All procedures were approved by the Regierungpräsidium Karlsruhe.

**Implantation of mini-osmotic pumps**

Mice were anaesthetized with isofluorane and a mini-osmotic pump (Alzet Model 1007D, Brain infusion Kit 3) with a volume of 100 µl and a flow rate of 0.5 µl/h containing different antibodies was implanted 1.1 mm lateral and 0.5 mm posterior to the bregma according to the manufacturer's instructions.

**BrdU**

BrdU (Sigma) was dissolved in 0.9% saline solution at 10 mg/ml and was heated at 50$^{o}$C until it was completely dissolved. For intraperitoneal injections (I.P) appropriate amount of BrdU was administered to match the concentrations indicated at Figure S5. For BrdU administration in drinking water, BrdU was dissolved in water with 0.1% sucrose in a concentration of 1 mg/ml. For embryonic labeling timed-pregnant TLX-CreER$^{T2}$YFP mothers were injected with two shots of BrdU (50 mg/kg) six hours apart at embryonic day 14 (E14).

**Temozolomide (TMZ) treatment**

Temozolomide dissolved in 75% saline 25%DMSO (or 0.9% saline in control animals) was injected daily I.P. in a concentration of 100mg/kg. BrdU was administered I.P. at 100mg/kg and mice were sacrificed 2 hours after injection or as indicated in the protocol.

**Tamoxifen**

TLX-CreER$^{T2}$YFP pups embryonically labeled with BrdU, were given two shots of Tamoxifen (Sigma-Aldrich, 83.35 mg/kg, 9 Sunflower seed oil:1 100% EtOH) 12 hrs apart from postnatal day 28 till 32.

TLX-CreER$^{T2}$YFP mice 2, 7 and 22 MO were given two shots of Tamoxifen (50mg/kg) 12 hrs apart for 5 days.

**Treatments with neutralizing antibodies**

Mini-osmotic pumps were filled with 100 µl of neutralizing antibodies or isotype controls at the following concentrations: for sFRP5 neutralization 333 µg/ml of Mouse IgG2B Isotype control (Novus, MAB0041) or anti-sFRP5 (Novus, MAB6266) dissolved in PBS were used. For CXCL10 neutralization 500 µg/ml Purified Armenian Hamster IgG Isotype control (Biolegend, 400902) or Armenian Hamster anti-CXCL10 from Urs Christen were used.

**FACS analysis and sorting**

Generation of single cell suspension and stainings for FACS analysis or FACS sorting were performed as described in (Llorens-Bobadilla et al., 2015). Briefly, mice were sacrificed, SVZ was microdissected and single cell suspension was obtained using the Neural Tissue Dissociation kit with Trypsin (or Papain when staining for CD31+ and CD11b+ cells) and Gentle MACS dissociator (Miltenyi). For staining the following antibodies were used: Ter119 APC-Cy7 (Biolegend, 1:100), O4 APC and APC-Cy7 (Miltenyi, 1:50), CD45 APC-Cy7 (BD, 1:200), GLAST (ACSA-1)-PE and APC (Miltenyi, 1:20), Prominin1-APC and PerCP-eFluor 710 (eBioscience, 1:75), Alexa488::EGF (Life Technologies, 1:100), PSA-NCAM PE-Cy7 Miltenyi, 1:75), CD31-PE (BD, 1:100), CD11b-APC (BD, 1:100) and Sytox Blue (Life Technologies, 1:1000).

**Time-lapse video microscopy**

Sorted quiescent and active NSCs from 2 and 22 MO mice were plated and tracked. *Ex vivo* activation of quiescent NSCs was rare. Hence our analysis was restricted to aNSCs. Video microscopy of primary adult neural stem cell cultures was performed with a Cell Observer (Zeiss) at constant conditions of 37 °C and 8% $CO_2$ as previously described (Ortega et al., 2013). Phase contrast images were acquired every 5 minutes for 5-6 days using a 20 X phase contrast objective (Zeiss) and an AxioCamHRm camera with a self-written VBA module remote controlling Zeiss AxioVision 4.7 software (Rieger et al., 2009). Time-lapse videos were assembled by using ImageJ whereas single-cell tracking was carried out using a self-written computer program (TTT) (Hilsenbeck et al., 2016).

**Immunostainings**

Mice were transcardially perfused with ice cold HBSS and 4% PFA. Brains were post-fixed in 4% PFA O/N and subsequently immersed in 30% sucrose. 15 µm sections were prepared using a cryotome. For stainings of E-LRCs, 50 µm sections were prepared at the vibratome. Sections were blocked for unspecific labeling in 0.25% Triton X-100, 3% horse serum for 1 hr at RT and consequently with primary antibody mix at 4°C O/N. Sections were washed and incubated with secondary antibodies in blocking buffer for 90' at RT. Primary antibodies used were: anti-DCX (guinea-pig, Merck Millipore, 1:1000), anti-GFP (chicken, Aves, 1:1000), anti-Sox2 (goat, Santa Cruz, 1:500), anti-BrdU (rat, abcam, 1:100), anti-S100b (rabbit, abcam, 1:100), anti-GFAP (rat, thermo fischer, 1:1000), anti-Ki67 (rabbit, novus, 1:200), anti-IL33 (goat, novus, 1:150). 4-8 sections, 6 sections apart were used for immunostainings.

**Cells**

Labtek chambers were coated with PDL/laminin and NSCs were seeded at a density 20000/cm$^2$ and treatments followed. Cells were blocked for unspecific staining in 0.25% Triton X100, 3% horse serum for 30' at RT and consequently with primary antibody mixture containing anti-beta III-tubulin (mouse IgG2b, Sigma, 1:300), anti-GFAP (mouse IgG1, Sigma, 1:800), anti-NG2 (rabbit, Millipore, 1:500) at 4°C O/N.

**Isolation and cultivation of NSCs in vitro**

SVZ was microdissected and single cell suspension was prepared using the Neural Tissue Dissociation kit with Papain (Miltenyi). Cells were transferred in Neurobasal A (NBM A) medium containing 2% B27 supplement serum (Gibco), 1% L-Glutamine, 2 µg/ml of Heparin, 20 ng/µl of human FGF basic growth factor (ReliaTech), 20 ng/µl of human EGF (Promokine). Cells were not used for longer than 10 passages. For treatment with recombinant mouse interferons α/β, 160 U/ml (Millipore) were added in NSC medium and cells were incubated for 48 h.

**Luciferase Reporter (Topflash) assays**

Luciferase reporter assays were performed as previously described (Berger et al., 2017).

Briefly, HEK293T cells were grown in 96-well plates and transfected with 5 ng Topflash, 1 ng Renilla and 44 ng empty vector (pCS2+) DNA using X-tremeGene 9

transfection reagent (Roche) and following the supplier's protocol. 24 h after transfection, cells were stimulated with the indicated conditions: CHAPS control or recombinant Wnt3a protein (Peprotec, 180 ng/mL) with or without recombinant sFRP5 protein (Novus, 5 µg/mL). To examine if neutralizing sFRP5 antibody can inhibit recombinant sFRP5, recombinant Wnt3a together with sFRP5 and the neutralizing antibody (Novus, 5 or 25 µg/mL) were pre-incubated at room temperature for 30 minutes before applied to the cells. After 24 h, cells were harvested and Luciferase activity was determined following the manufacturer's manual (Promega, Dual-Luciferase Reporter Assay System). Values are presented as Firefly activity normalized to Renilla values.

**Sphere assay**

aNSCs (CD45-O4-Ter119-GLAST+CD133+EGFR+) (Figure S6A) from 2, 7 and 22 MO were sorted in 96 wells containing 3x growth factors and the diameter of spheres was measured 5 days later using a LEICA table microscope.

**Comet assay**

qNSCs (CD45-O4-Ter119-GLAST+CD133+EGFR-) and aNSCs (CD45-O4-Ter119-GLAST+CD133+EGFR+) (Figure S6A) were isolated in NBM A with B27 and comet assay was performed as described in (Walter et al., 2015) with the difference that low-melting-temperature agarose was purchased from Biozym.

**Microscopy**

Confocal images were acquired with a LEICA SP5 microscope with a 405 nm laser, an argon multiline (458-514 nm), a helium neon 561nm and a helium neon 633nm laser. For quantification of stainings of vibratome sections we acquired tilescans from the whole ventricle and z-stacks of 20 µm with 1 µm apart in a resolution of 2048x2048. For quantification of cryosections we acquired tilescans of the whole ventricle combined with z-stacks covering the tissue thickness in a resolution of 1024x1024. Finally, for imaging of stained cells from in vitro cultures 6-12 fields of view were obtained at a resolution of 512x512. For all images a 40x oil immersed objective was used. Quantifications were performed with Fiji and the plug-in cell counter navigating through the stacks. For quantification of TCF/Lef activity in different domains, we measured the total length of the SVZ occupied by cells and assigned the upper 1/3 as dorsal and the lower 2/3 as lateroventral. Highly

autofluorescent speckles called lipofuscin were observed in the aging brain. Speckles present in all fluorescent channels were visually excluded during quantifications.

**Analysis of Smart-seq2 single-cell RNA-seq data**

**Sorting for Smart-seq2**

Preparation was performed as described in (Llorens-Bobadilla et al., 2015). Briefly, we sorted for CD45-O4-CD133+GLAST+ NSCs (Figure S6A). Single NSCs were handpicked and libraries according to Smart-seq2 were prepared. 4 mice of 23 MO were pulled per replicate.

In total, we performed RNA-seq on 145 old single cells in parallel with published data from (Llorens-Bobadilla et al., 2015) which were used as young counterparts. All the steps for cell sorting and library preparation were identical. Through quality control steps, we removed 12 cells and kept 133 cells for downstream analysis. For isolation of astrocytes, we sorted for GLAST+O4-CD45- from cortex or striatum, cells were handpicked and libraries were prepared according to Smart-seq2 as previously described in (Llorens-Bobadilla et al., 2015).

Quality control steps are described as following.

**Smart-seq2 library preparation**

Single cell RNA-seq libraries were prepared according to the Smart-seq2 protocol as described by (Picelli et al., 2014). Single cells were pipetted in lysis buffer and were frozen O/N. Subsequently, cells were thawed and reverse transcription was performed with an oligo(dT) primer and a locked nucleic acid-containing template-switching oligonucleotide. ERCC Spike-Ins (Ambion) were added to 8 randomly selected samples at a dilution 1/1000000. Full-length cDNA was amplified with the KAPA HiFi polymerase by 20 cycles of PCR. Samples with high quality of cDNA were further processed after assessment on a High Sensitivity Bioanalyzer chip (Agilent). Libraries for Illumina sequencing were generated with the Nextera XT Sample preparation protocol after extending the tagmentation to 8 minutes and doing a double bead clean up with 0.8X AMPure XP SPRI beads after PCR amplification of 9 cycles.

**Read trimming and mapping**

Raw read quality was checked by FASTQC (http://www.bioinformatics.babraham.ac.uk/projects/fastqc/). Trimming of adapter

sequences in raw reads was performed before alignment with Btrim64 (http://graphics.med.yale.edu/trim) (Kong, 2011). Mapping of trimmed reads to the mouse genome (ENSEMBL Release 78/GRCm38.p3) was done using STAR 2.4.0g (Dobin et al., 2013). Mapping results to the genome were visually inspected with the Integrative Genome Viewer (www.broadinstitute.org/igv/).

**RNA-seq data quality metrics**

RNA-seq data quality metrics of each cell, including total reads, transcriptome mapped reads and transcriptome mapped rate was calculated by picard-tools-1.123 (https://broadinstitute.github.io/picard/) (Table S4).

**Gene Expression Matrices**

Gene expression matrices were generated as previously described (Shalek et al., 2014; 2013). Gene expression levels as transcripts per million (TPM) and fragments per kilobase of transcript per million mapped reads (FPKM) were produced with RSEM 1.2.18 with default parameters. Additionaly, we used Trinity (Haas et al., 2013) (http://trinityRNA-seq.github.io/) based on edgeR (Robinson and Oshlack, 2010) to perform TMM (trimmed mean of M-values) an additional normalization on FPKM (abbreviated TMM-FPKM), to be able to compare samples with differences in the total cellular RNA production.

**Quality control of single-cell RNA-seq data**

The qualities of single cell RNA-seq libraries were checked by the combination alignment rates and number of genes detected with TPM >1. Cells showing substantially fewer numbers of genes detected (TPM >1) and/or lower mapping rates (two times standard deviation) than others were filtered out. We also filtered out cells in which Gapdh and Actb are lowly expressed (TPM <100) and Slc1a3-negative NSCs (TPM <10). In total, 132 single cells passed quality control and were used in downstream analysis.

**ERCC spike-in controls**

The quality of single-cell RNA-seq data was assessed by adding known amount of 92 ERCC spike-in RNA transcripts in 8 random cells and the expression levels of these transcripts in TPM correlated well to the known amount.

**Monocle pseudotime assignment**

The TPM values data from young and old cells were loaded together into the monocle2 R package using its relative2abs function (Qiu et al., 2017). During the creation of the CellDataSet object lowerDetectionLimit was set to 0.5 and a negbinomial expression family was selected. The ordering genes used for the pseudotime calculation were selected based on a mean_expression >= 0.5 and dispersion_empirical >= 3 * dispersion_fit. Pseudotime assignments for all cells were saved into a file for later use.

**Expression of DNA damage associated genes**

To check for the expression of DNA damage associated genes in the data, a heatmap was created using the pheatmap R package (version 1.0.8) from a list of manually selected genes. The TPM values for those genes were log2 transformed before plotting

**PCA**

PCA was run on the TPM values of the 2000 most variable genes in the dataset and for all cells PC1 and PC2 were plotted against each other in a scatterplot. PCA plots were also prepared for individual subpopulations and cells colored by age of the animal.

**DE analysis Smart-seq2**

Differentially expressed genes between astrocytes and qNSC1 were determined using a likelihood ratio test as described in (Llorens-Bobadilla et al., 2015). The log-transformed TPM gene expression values of the up and downregulated genes (>2 fold-change, adjusted p-value <0.1) from qNSC1, qNSC2 and astrocytes in the Smart-seq2 data were plotted as a heatmap (using pheatmap R package).

Differentially expressed genes of each activation state against all others were determined by t-test as provided by Seurat. Differentially expressed genes between cells from old and young mice within each activation state were determined by DESeq2 after exclusion of non-expressed genes. In addition, we calculated differentially expressed genes between cells from old vs. young mice within each activation state by the difference of the mean log-transformed TPM expression values divided by the mean SD and ranked by the nominal p-value (t-test).

**Euclidean distance calculation**

The euclidean distances between neighbouring activation states along the neurogenic lineage (qNSC1, qNSC2, aNSC1, aNSC2) between cells from 2 MO and 23 MO mice within the same subpopulations were calculated on the first 5 principal components and their distribution was plotted using density estimation (ggplot2 R package).

**Bulk RNA sequencing**

**Bulk RNA seq**

For Bulk sequencing we sorted 1000 events of different populations based on the following marker combinations: Endothelial CD45-CD31+, Microglia CD45+CD11b+, NSCs CD45-CD133+GLAST+, Neuroblasts CD45-GLAST-PSA-NCAM+ (Figure S6C). Since the CD31 epitope was sensitive to trypsin we did the endothelial and microglia cell isolation with the Neural Tissue Dissociation kit (papain). Briefly, RNA was isolated with arcturos pico pure kit and cDNA was prepared using the SMARTer Ultra Low Input RNA for Illumina Sequencing – HV. Finally, libraries were prepared for sequencing using the NEBNext Ultra DNA Library Prep Kit for Illumina. 2 2 MO and 4 19 MO mice were pulled per replicate.

**Processing RNA-seq data of bulk**

We prepared biological duplicates of libraries from young and old populations from NSCs, endothelial, microglial and neuroblast cell types. Quality control of cell population RNA-seq data was performed as the single-cell RNA-seq data. After quality control raw reads were mapped to the mouse reference genome GRCm38 (ENSEMBL release 78/ GRCm38.p3) using STAR_2.4.0g1. Genes annotated in ENSEMBL release 78 were quantified with HTSeq 0.6.1p2. Differential expression analysis was performed with DESeq2.

**GO term enrichment analysis**

The lists of differentially expressed genes from comparing old to young for NSCs, neuroblasts, microglia, endothelial cells were filtered for those genes with an adjusted p-value of less than 0.05 and then supplied to the clusterCompare and simplify functions of the clusterProfiler R package (Yu et al., 2012) to prepare a dotplot of the top 8 GO categories from each celltype using the “biological process” ontology.

**Expression of Innate immune response genes**

Significantly upregulated genes in the comparisons of 19MO to 2MO samples for each cell type were checked for annotation in the InnateDB and Ensembl gene IDs were obtained using the biomaRt R package (version 2.32.1). The annotated genes were highlighted on MA plots of the comparisons for the respective celltypes. In the 7MO to 2MO NSC MA plot the genes from the 19MO vs 2MO comparison were highlighted.

**10x Chromium 3′ sequencing**

**Sorting for 10x Chromium 3′**

Single cell suspension was prepared as described before. To ensure that there is enough starting material for the Chromium 3' 10x platform, we sorted CD45-O4-Ter119-GLAST+ (Figure S6B). 8000 FACS events underwent the downstream process according to the manufacturer's details. 4 2MO and 8 22 MO mice were pulled for each library.

**Library preparation, sequencing and mapping**

We prepared one library from cells isolated from old and another with cells isolated from young mice (both with 10x Genomics Chemistry: Single Cell 3' v2) and sequenced them on a HiSeq 4K PE 100. The Cell Ranger Software (Ver. 2.0.0) provided by 10x Genomics was used to map the reads (provided as fastq files) to the mouse reference genome (ENSEMBL Release 78/GRCm38.p3) for each sample individually and the two samples were merged according to the Cell Ranger manual.

**Analysis with the Seurat package**

The Seurat R package (version 2.2.0) was used for further inspection and data analysis. First all genes, which showed expression in less than 3 cells were discarded. Then the cells were filtered for further analysis based on the following parameters: expression of at least 1500 genes and at most 4500 genes (to exclude cell duplets), less than 10% of transcripts coming from mitochondrial genes. After these filters 3066 cells remained (out of 3937 cells initially provided by the CellRanger pipeline) (Table S4). The transcript counts were log transformed, the number of detected genes, number of detected unique molecular barcodes (UMIs) and the percentage of mitochondrial gene expression was regressed out and transformation to z-scores was performed, by subtraction of the mean and division by the standard deviation. As we

compared cycling and non-cycling cells we aimed to reduce the influence of the cell cycle states on cells from the same cell type, while keeping the cell cycle signal, which is an important component of NSC activation. As described in the Seurat package documentation, all cells were scored for the cell cycle states G1-, G2/M- and S-phase and then the difference between the G2/M- and S-phase scores was regressed out to discard the cell cycle states difference, while keeping the cell cycle signal. Genes were determined to be variable based on the following parameters: mean expression between 0.0125 and 4 and log variance to mean ratio of at least 0.5. Those variable genes were used as input for PCA. This dimensionally reduced data was used for clustering using Seurat's graph-based clustering approach with a resolution parameter of 0.8, selecting the first 8 principal components as input. 18 cells were excluded from the further analysis as they also showed expression of the leukocytic marker gene PTPRC (CD45) or ependymal marker genes (Jacquet et al., 2009) and thus are possibly contaminations of cells from these celltypes. For visualisation t-SNE was run on the first 8 principal components. To check whether clusters were separating based on the age of the animals and if there are batch effects, PCA and t-SNE plots were generated for all cells and individual subpopulations and cells were colored according to the animal age (Figure 4C). Gene expression of individual marker genes in the determined clusters was checked by coloring the cells in the t-SNE plot according to gene expression strength. The identity of the subpopulations was determined by manual inspection of the gene expression values for previously used marker genes and comparison of differentially expressed genes of each cluster (compared to all the other clusters in the dataset). Those were compared to differentially expressed genes from the Smart-seq2 single-cell RNA sequencing data (Llorens-Bobadilla et al., 2015). The aNSC0 subpopulation is composed of two clusters which showed a difference in the expression of immediate early response genes, while the aNSC1 subpopulation contains two clusters showing a seperation based on the predicted cell cycle phase. A phylogenetic tree based on average cells for all determined identities was constructed based on the first 8 PCs using the BuildClusterTree function. The average gene expression for all genes was calculated between young and old cells in NSCs, cell types along the neurogenic lineage as well as OPCs and ODs and plotted in a scatterplot with log10 transformed axes.

**Monocle pseudotime assignment**

Raw transcript counts from the CellRanger output were also loaded into the monocle2 R package (version 2.4.0) and filtered to exclude cells identified as OD or OPCs. A cellDataSet object was prepared as described for the Smart-seq2 sequencing data. The ordering genes were selected to have a mean expression >= 0.6 and an empirical dispersion >= 3 * dispersion fit. Pseudotime computation results were saved and used together with the cluster identities from the Seurat clustering to check if the identified clusters agree with the predicted pseudotime by plotting the identity-colored cells according to their monocle predicted reduced dimensions dimensions and vice versa coloring cells in the tSNE plot by their predicted pseudotime value.

**DE and GO term enrichment analysis**

To find differentially expressed genes between cell from 2 and 22 MO mice the DESeq2 R package (version 1.16.1) was used. The clusterProfiler R package (version 3.4.4) was used for GO term enrichment analysis with its clusterCompare and simplify functions using the "biological process" ontology. Genes with an adjusted p-value <0.05 and an absolute Fold Change >2 were used. Differentially expressed genes of each activation state against all others were determined by t-test as provided by Seurat. DE genes between cells from old and young mice within each activation state were determined by DESeq2 as provided by Seurat. In addition, we calculated differentially expressed genes between young vs. old cells within each activation state by the difference of the mean log-transformed expression values divided by the mean SD and ranked by the nominal p-value (t-test).

**Euclidean distance calculation**

The euclidean distances between neighbouring activation states along the neurogenic lineage (qNSC1, qNSC2, aNSC0, aNSC1, aNSC2, TAP, NB) as well as between qNSC1 and OD or between cells from 2MO and 22MO mice within the same subpopulations were calculated on the first 8 principal components and their distribution was plotted using density estimation (ggplot2 R package).

**Statistics**

Statistics were performed as indicated in each figure. All multiple comparisons were performed with GraphPad Prism's one-way Anova function, which also performs a Tukey-Kramer test, reporting p values adjusted to control family-wise

error rate for the family comprising comparisons of each group against all other groups.

**Supplemental item titles**

**Data S1 Related to Figure 1**

Modeling the NSC Dynamics in the V-SVZ.

**Data S2 Related to Figure 6**

Markov chain-based computational method to identify niche determinants.

**TableS1_DE Genes in Celltypes_10x_and_Smart-seq2 Related to Fig. 3, 4, S3**

Lists of differentially expressed genes in each cluster when compared to all other clusters from Smart-seq2 and Chromium Single cell 3'. Gene ontology analysis included for each gene set.

**TableS2_Diff. Expressed Genes Fig. 3 and 5**

List of DE genes between 19 MO and 2 MO mice for NSCs, Neuroblasts, Endothelial and Microglial cells. Also contains the list of DE genes from the comparison between old qNSC1 vs old astrocytes from Smart-seq2 single cell RNAseq. Finally, contains the list of DE genes, as calculated by DEseq2 or mean diff./SD from the comparison of cells from old vs. young mice within each activation state, sequenced with Smart-seq2 or 10X. We remind the reader that for the single cell data the p-values should merely be taken as an aid to rank the gene and not as considered measures of statistical significance, as that would incorrectly assume that each individual cell is an independent sample.

**TableS3_Subpopulation Specific Signaling Intermediates Related to Figure 6**

Lists of signaling intermediates identified by the MCCM.

**Table S4_scRNAseq Quality Metrics Related Fig. 3, 4 and STAR methods**

RNAseq quality metrics of Bulk RNA seq and sc RNA sequencing with Smart-seq2 and 10x platforms. Also contains the number of cells per activation state for Smart-seq2 and 10x Chromium single cell.

Figure1

Click here to access/download;Figure;Figure1.jpg

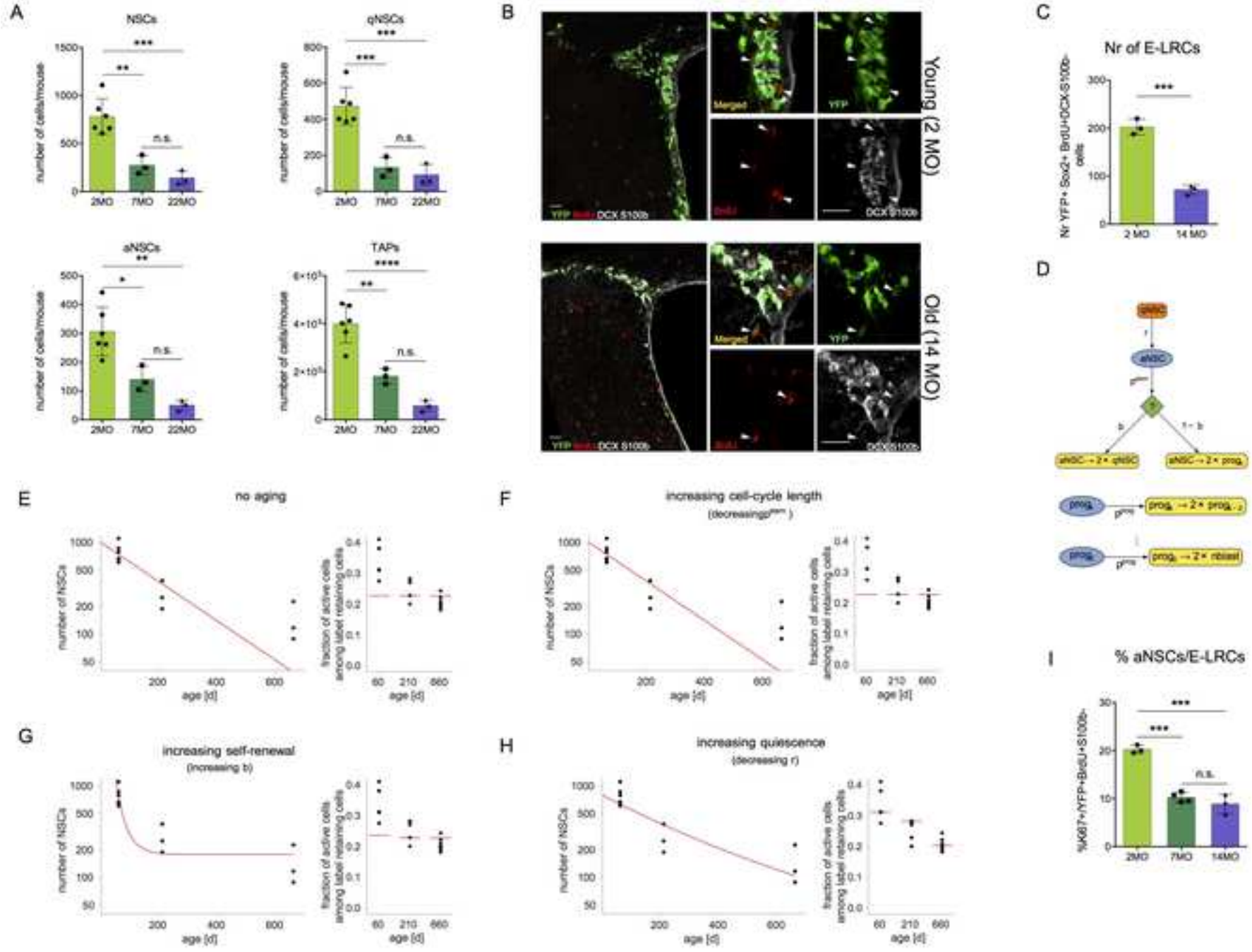

Figure2

Click here to access/download;Figure;Figure2.jpg

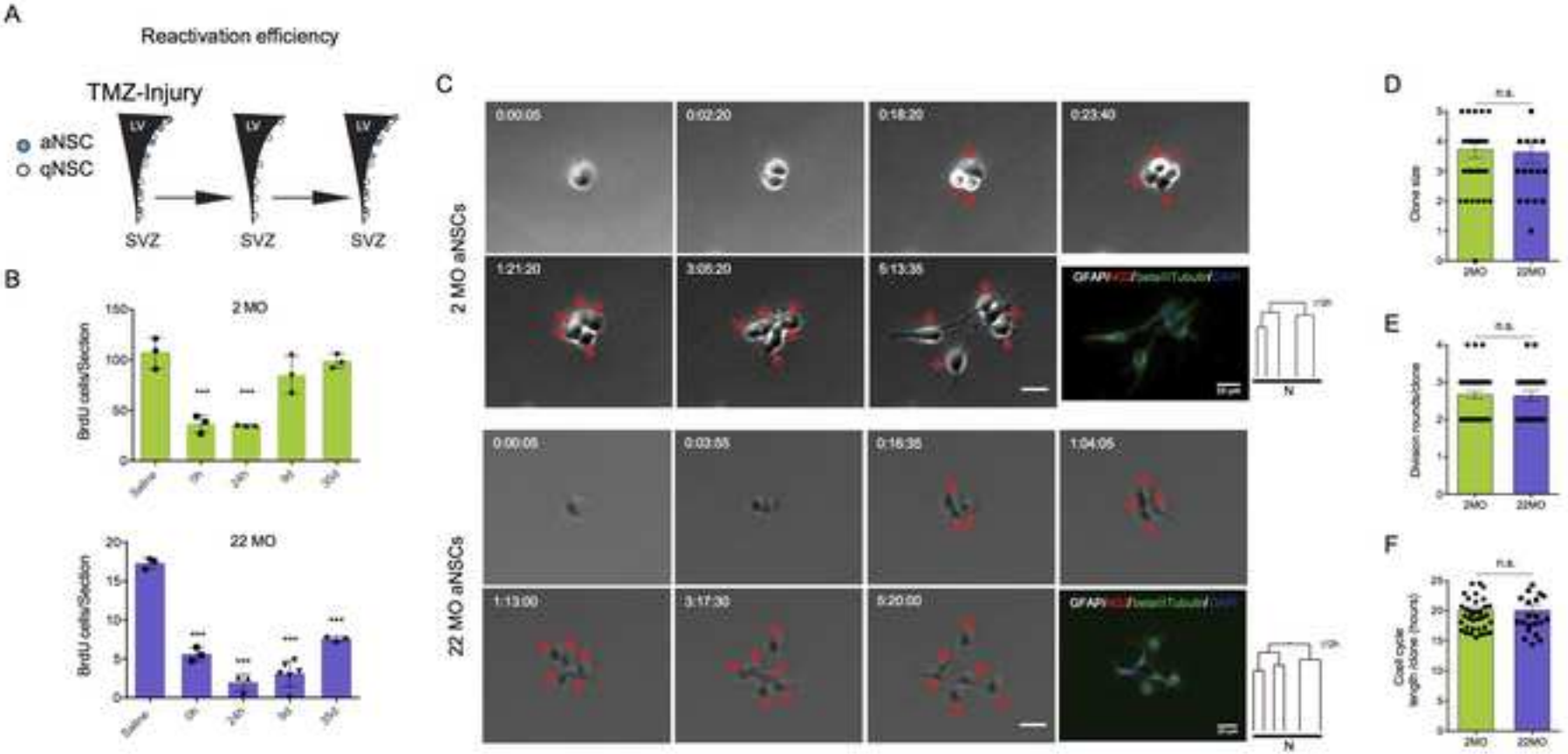

Figure3

Click here to access/download;Figure;Figure3.jpg

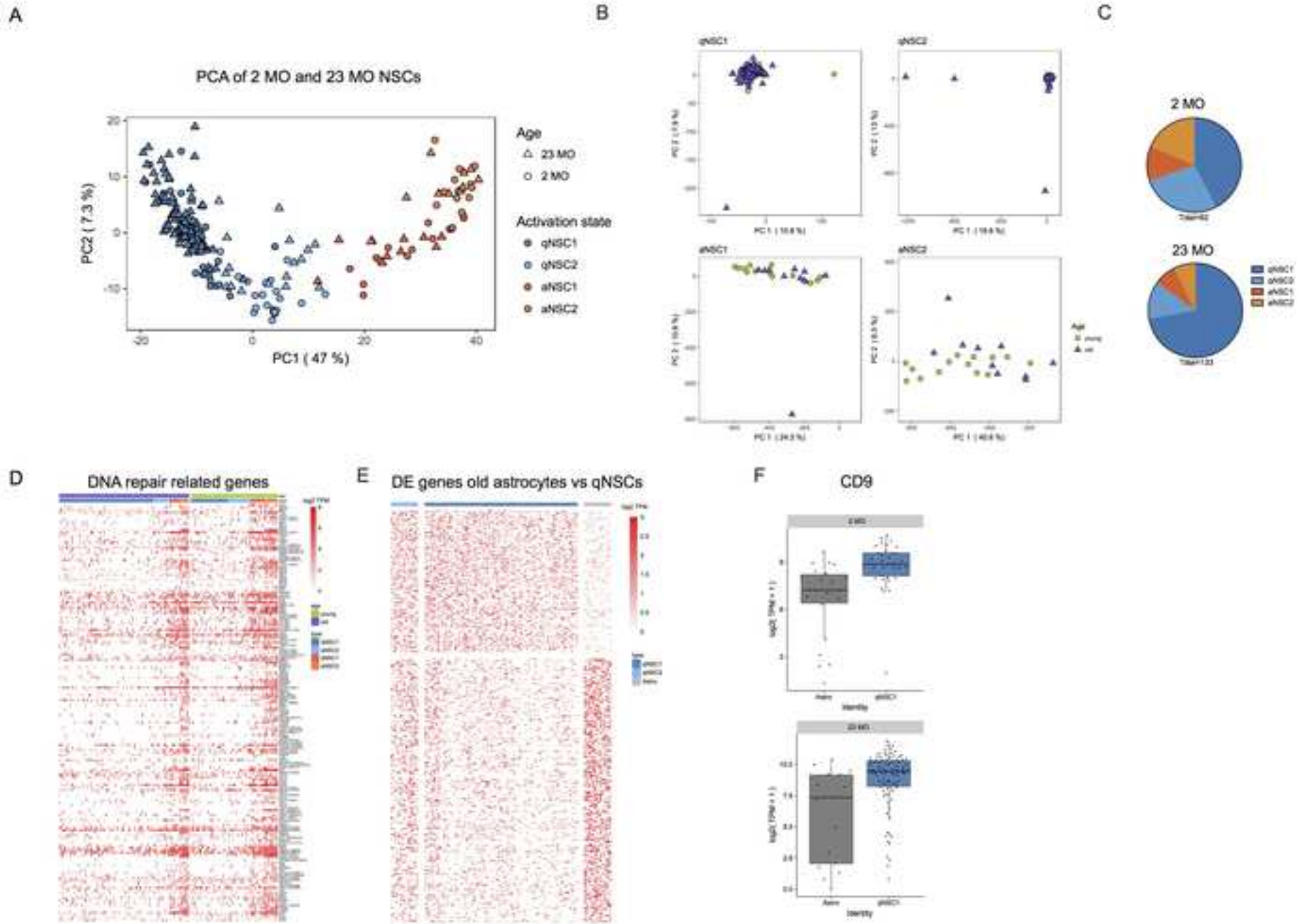

Figure4

Click here to access/download;Figure;Figure4.jpg

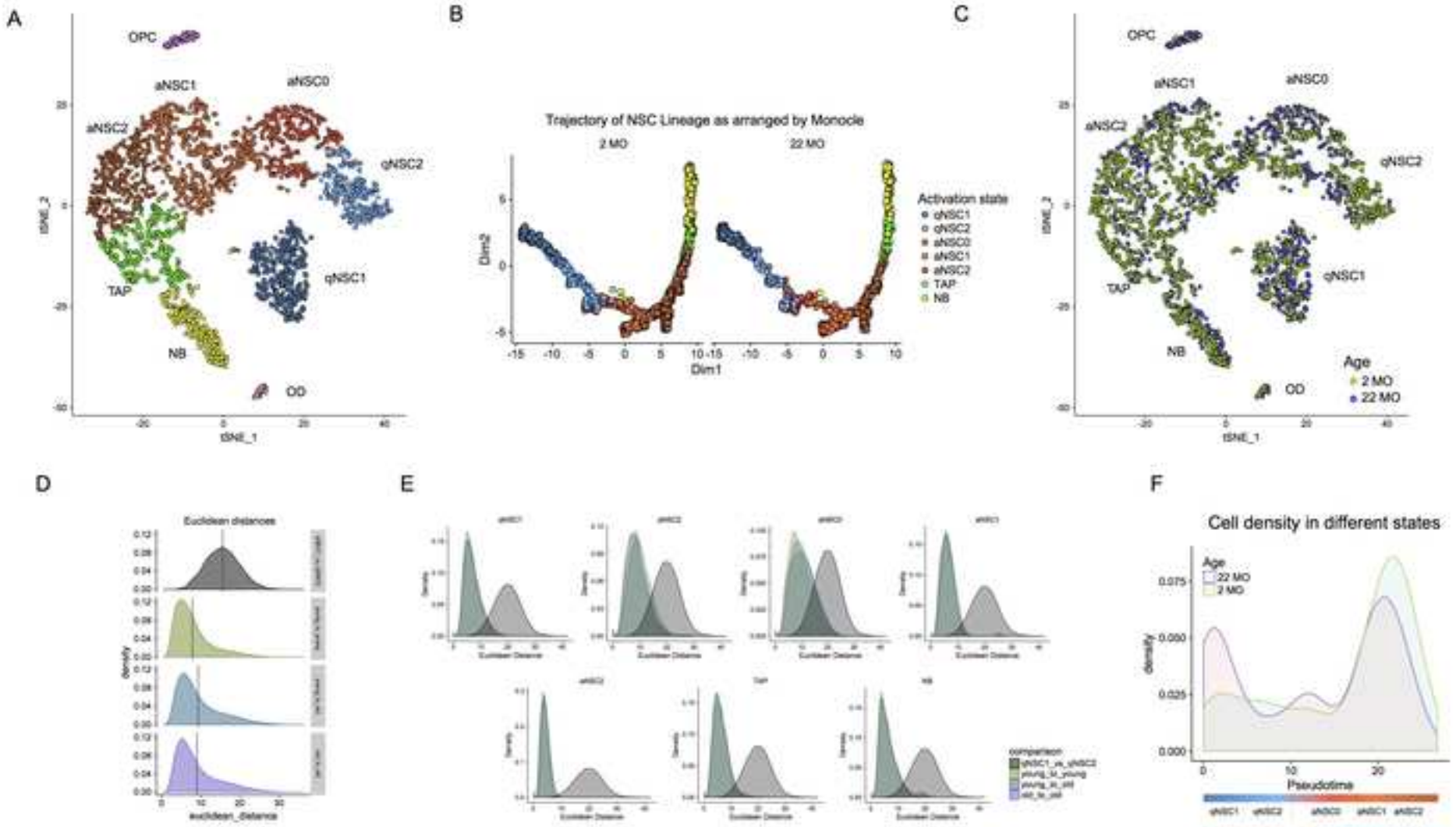

Figure5

Click here to access/download;Figure;Figure5.jpg

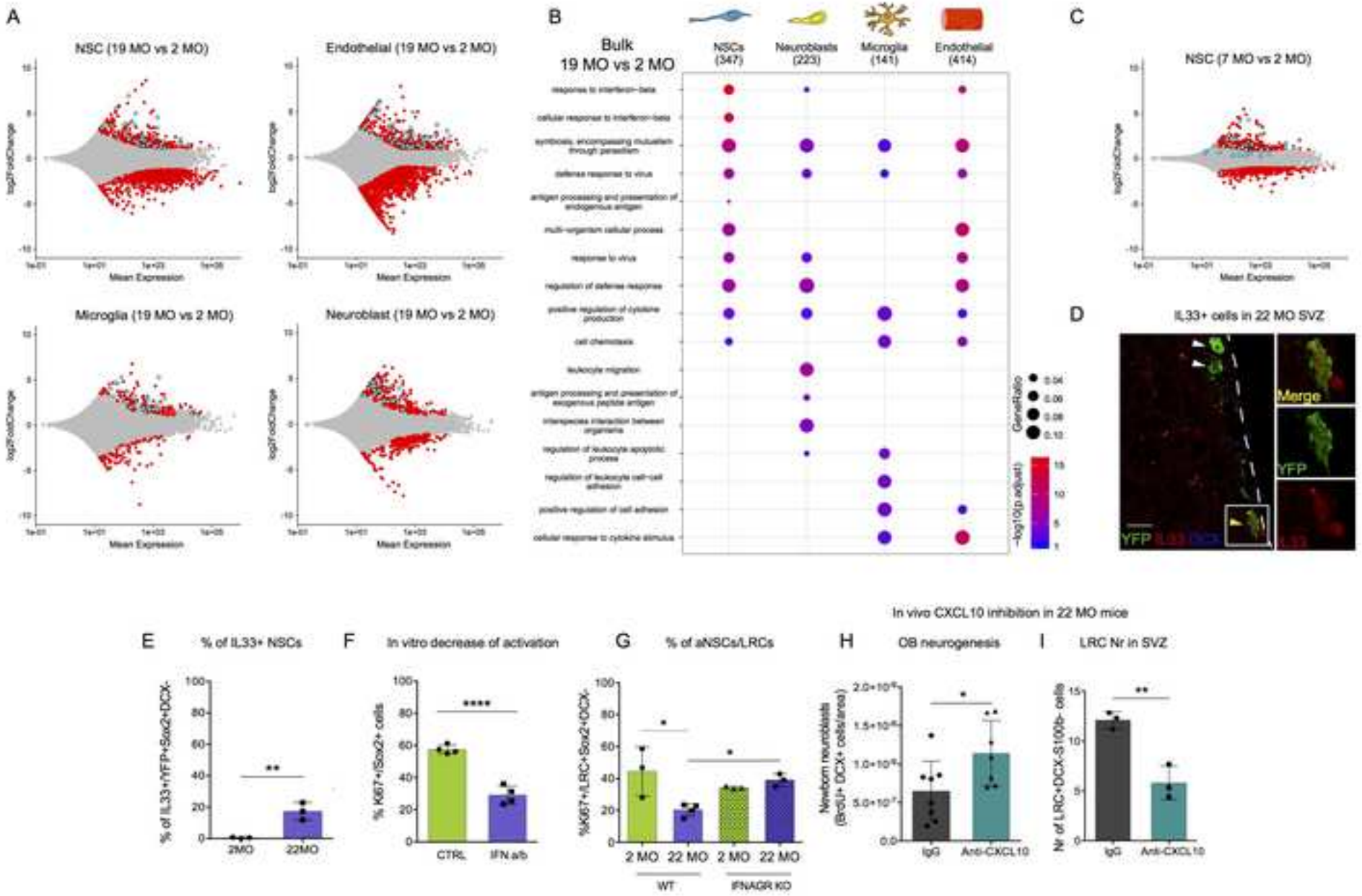

Figure6

Click here to access/download;Figure;Figure6.jpg

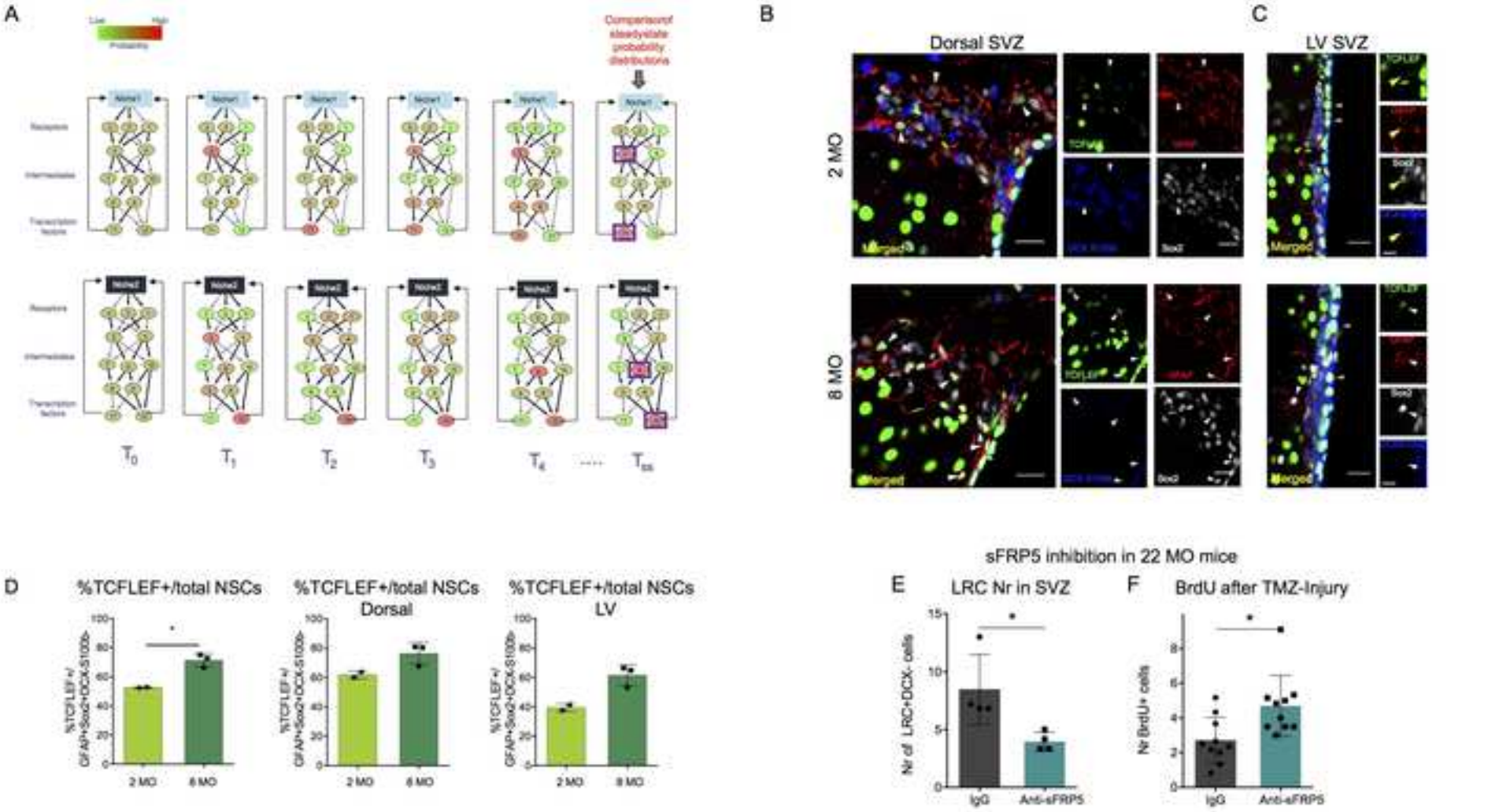

# Modeling the Dynamics of Neural Stem Cells in the Subventricular Zone (SVZ)

## 1 Development of the model with constant rates

We set-up and analyze a model of cell population dynamics in the subventricular zone (SVZ), capable of reproducing observed experimental data. The model accounts for dynamics of neural stem cells (NSCs) and progenitor cells. These dynamics have been experimentally addressed before, suggesting that NSCs exist in a quiescent or an active (dividing) state (Ponti et al., 2013, Calzolari et al., 2015, Lim et al., 2016). Dividing NSCs produce progenitors via symmetric divisions (Ponti et al., 2013, Lim et al., 2016) or undergo asymmetric divisions as well as symmetric self-renewing divisions (Calzolari et al., 2015). Moreover, progenitors have been observed to undergo 2-3 rounds of symmetric divisions (Ponti et al., 2013, Calzolari et al., 2015, Lim et al., 2016).

Following that experimental evidence, we propose a mathematical model of NSCs in the SVZ, in which quiescent NSCs (qNSCs) may enter the cell cycle to become active NSCs (aNSCs; Data S1-Fig.1.1). Active NSCs divide and become either two qNSCs or two progenitors with the capacity of performing $n$ symmetric self-renewing divisions. Taking into account the two division modes of stem cells provides a minimal set of assumptions allowing, on one hand,

to explain the age-related decline of NSC numbers, which has been observed in the data as well as in previous studies (Shook et al., 2012, Capilla et al., 2014, Silva et al., 2016) and, on the other hand, to fit the observation that NSCs that incorporated BrdU once become quiescent. Both observations could be also explained by replacing the symmetric self-renewal divisions, i.e. aNSC $\rightarrow 2 \times$ qNSC by asymmetric divisions of the form aNSC $\rightarrow$ progenitor + qNSC, or assuming co-existence of both types of divisions. Such assumptions lead to a similar model and it can be shown mathematically that both models are equivalent (with a different definition of model parameters). Also, introducing additionally cell death rates for all cell types or directly transitions of NSCs into a postmitotic non-neurogenic astrocyte would not change the model dynamics (Stiehl and Marciniak-Czochra, 2011, Ziebell et al., 2017). In summary, the model can be directly extended to account for fate possibilities different than symmetric division such as asymmetric divisions, cell death or direct transitions into astrocytes what would lead to an increase of the number of model parameters (hence a different quantification) but would not affect the dynamical aspects which are behind model conclusions. Such scenario has been considered recently in the model of hippocampal neurogenesis and showed consistent dynamics (Ziebell et al., 2017). Taking it into account, in the reminder of this paper we consider the model based on a minimal set of assumptions accounting for experimentally observed types of divisions and cell transitions. A corresponding scheme representing rules of the stem cell system is presented in Data S1-Fig.1.

Taken together, our model consists of the set of linear ordinary differential equations

$$\begin{aligned}
\frac{\mathrm{d}}{\mathrm{d}t}\,\mathsf{qNSC}(t) &= -r\mathsf{qNSC}(t) + 2bp^{\text{stem}}\mathsf{aNSC}(t),\\
\frac{\mathrm{d}}{\mathrm{d}t}\,\mathsf{aNSC}(t) &= r\,\mathsf{qNSC}(t) - p^{\text{stem}}\mathsf{aNSC}(t),\\
\frac{\mathrm{d}}{\mathrm{d}t}\,\mathsf{prog}_n(t) &= -p^{\text{prog}}\,\mathsf{prog}_n(t) + 2(1-b)p^{\text{stem}}\,\mathsf{aNSC}(t),\\
\frac{\mathrm{d}}{\mathrm{d}t}\,\mathsf{prog}_k(t) &= 2p^{\text{prog}}\mathsf{prog}_{k+1}(t) - p^{\text{prog}}\mathsf{prog}_k(t),
\end{aligned} \tag{1.1}$$

$k \in \{0, \ldots, n-1\}$, where $r$ is the activation rate of qNSCs, $p^{\text{stem}}$ the division rate of NSCs, $b$ the probability of an aNSC to divide into two qNSCs versus two progenitors. The parameter $p^{\text{prog}}$ denotes the division rate of progenitors and $n \in \mathbb{N}$ the total number of division rounds of a progenitor, and $t$ is the age of the animal.

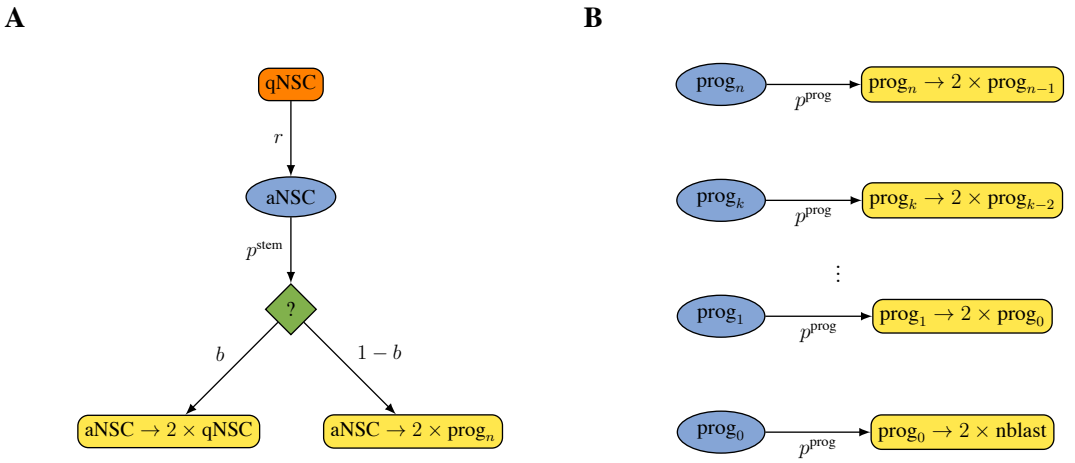


Data S1-Fig. 1: **Graphical representation of the proposed model**

(**A**) Quiescent neural stem cells (qNSCs) may enter the cell cycle at the rate $r$ to become activated NSCs (aNSC), which in turn divide at the rate $p^{\text{stem}}$ to either produce two qNSCs (with probability $b$) or two progenitors (with probability $1-b$) with the capacity of $n$ symmetric self-renewing division ($\text{prog}_n$). (**B**) Progenitors with capacity of $k$ symmetric self-renewing divisions ($k = 1, \ldots, n$) divide at the rate $p^{\text{prog}}$ into two progenitors with capacity of $k-1$ symmetric self-renewing divisions and progenitors without this capacity ($\text{prog}_0$) symmetrically divide into two neuroblasts.

Since we solely focus on the dynamics of NSCs, we follow a top-down approach in which we start with a basic model which is capable of reconstructing the produced data. Thus, instead of considering the hypothesis of Ponti et al, 2013, that progenitors perform 3 symmetric self-renewing divisions followed by direct transformation into neuroblasts, we equivalently assume that progenitors undergo $n = 2$ symmetric self-renewing divisions followed by symmetric division into neuroblasts. These neuroblasts then enter the rostral migratory stream and move away from the SVZ. This approach allows eliminating one model parameter (transformation rate into neuroblasts) while maintaining the total number of progenitor division rounds.

# 2 Model quantification

The cell cycle dynamics of NSCs and progenitors were investigated in the study of Ponti et al, 2013. Average cell cycle and S-phase lengths of both cell types have been measured as $t_c^{\text{stem}} = 17.5\,\text{h}, t_s^{\text{stem}} = 4.4\,\text{h}, t_c^{\text{prog}} = 20.5\,\text{h}$ and $t_s^{\text{prog}} = 13.5\,\text{h}$. To compute the proliferation rate of NSCs and progenitors, we interpret cell cycle lengths as doubling times of the corresponding exponential growth processes, leading to

$$p^{\text{stem}} = \frac{\log(2)}{t_c^{\text{stem}}} \text{ and } p^{\text{prog}} = \frac{\log(2)}{t_c^{\text{prog}}}. \tag{2.1}$$

The remaining parameters $r$ and $b$ are estimated by fitting the model to data, consisting of measurements of the number of NSCs (data in Fig.1), the relative frequency of the active cells ($\text{Ki67}^+$) as a fraction of the adult label-retaining cells and the relative frequency of the active cells (2h BrdU) as a fraction of the TLX labelled cells. For a mathematical explanation of how to simulate the relative frequency of active label-retaining cells, we refer the reader to Section 5. Model fitting is obtained using the NonlinearModelFit procedure of Mathematica 9 to numerically minimize the weighted sum of squared residuals. Weights are chosen as inverse squares of the standard deviation. The resulting fit of model (1.1) to the experimental data is presented in Fig.1E.

To increase the number of data points used for model fitting, we consider a joint data set consisting of the subset of the frequency of active cells as a fraction of the adult label-retaining cells and of the subset of active cells as a fraction of the TLX labelled cells (data shown in

Fig.S1 A-D, Fig.S5). We fit the model using both subsets simultaneously. In Section 6 we show the fits that are obtained if the relative frequencies of subset 1 (active adult label-retaining cells) only or subset 2 (active TLX labelled cells) only are used to represent the fraction of active NSC. The results obtained based on the different data sets are consistent and lead to the same conclusions.

# 3 Evaluation of the model with constant rates

Although the model with constant parameters reflects decay in the number of NSCs, we observe that it does not match the long time dynamics which exhibits a decay-saturation with age (shown in Fig.1E in logarithmic scale). This result is in agreement with results obtained for the model of hippocampal neurogenesis (Ziebell et al., 2017). To explore further discrepancy between model (1.1) and experimental data, we observe that in a model with constant parameters given by system (1.1) the fraction of qNSCs to aNSCs converges rapidly to a constant value. The limit $\lim_{t\to\infty} \frac{\mathsf{qNSC}(t)}{\mathsf{aNSC}(t)}$ can be calculated from a corresponding differential equation for $\frac{\mathsf{qNSC}(t)}{\mathsf{aNSC}}$ (Ziebell et al., 2014). It yields that also the predicted relative frequency of the aNSCs as a fraction of all NSCs remains constant in time (Fig.1E), which does not match the data exhibiting a decline of the respective fractions during aging. This observation motivates us to search for mechanisms that can explain the age-related changes in stem cell dynamics.

# 4 Model of aging

Model (1.1) consists of 3 NSC related parameters, $r$, $b$ and $p^{\text{stem}}$. In order to investigate how the dynamics of NSCs change during aging, we consider three scenarios, each related to a time-depended change of one of the three parameters. Considering the different scenarios leads to three models with time-dependent parameters, which are validated using the above described different sets of experimental data. Parameter values obtained for the three fits are listed in Data S1-Tables 1, 2 and 3 in Section 6 and corresponding plots are presented in Data S1-Fig.5 through Fig.15.

## 4.1 Model with cell cycle lengthening

The first scenario, ***cell cycle lengthening***, assumes that an aNSC takes on average progressively longer to complete its cell cycle. Since the cell cycle length enters the model via formula (2.1), its increase is modelled by decreasing in time the aNSC division rate ($p^{stem}$) and cell cycle lengthening is implemented using

$$p^{\text{stem}}(t) = p^{\text{stem}}_{\text{max}} e^{-\beta_p t}.$$

Changing the cell division rate of aNSCs does not, however, change the dynamics of the predicted relative frequency of the aNSCs as a fraction of all NSCs (see Fig.1F) which remains constant in time. The best fit also does not exhibit the saturation observed in data (Fig.1F), since the parameter estimation results in a very small value of $\beta_p$.

## 4.2 Model with increasing self-renewal

The second scenario, ***increasing self-renewal***, is based on the hypothesis that during aging, the fraction of self-renewing aNSCs divisions increases, i.e., a higher fraction of divisions leads to two qNSCs than to two progenitors. This is modeled by a time-dependent parameter $b$,

$$b(t) = \frac{1}{2}\left(1 + e^{-\beta_b t}(2b_{\text{min}} - 1)\right).$$

The specific choice of the function $b(t)$ is motivated by the observed decline of NSC counts during aging, i.e. $b(t) \leq 1/2$ must hold. The chosen function can be fitted to satisfy this condition for any $b_{\text{min}} \leq 1/2$.

The resulting increased production of qNSCs yields a slightly increased frequency of qNSCs as a fraction of all NSCs and consequently, a decrease in fraction of aNSCs of all NSCs. However, the latter decline is very small (only 3.5%) not matching the decline observed in the experimental data (Fig.1G) and, in particular, too small in young mice. Moreover, the resulting dynamics involves a very rapid decline of aNSCs at young age. Following the dynamics of the model for small times (time going back to zero), the model predicts a three order of magnitude larger NSCs population at the initial time, i.e. around $1.1 \times 10^6$ NSCs at time zero, what seems to be unrealistic (see Data S1-Fig.2).

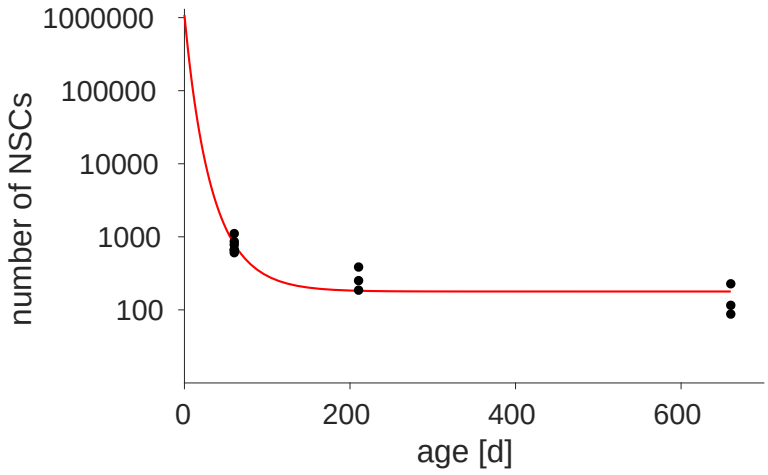


Data S1-Fig. 2: Fit of the neurogenesis model with increase of self-renewal during aging. The cell counts at age 0 are in the order of $10^6$. The red curve corresponds to model simulations. Each black dot denotes experimental data of one mouse.

## 4.3 Model with increasing quiescence

Finally, we model ***increasing quiescence*** by assuming that NSCs spend progressively longer time in the qNSCs stage during aging. It is modelled using a time-declining activation rate,

$$r(t) = r_{\max} e^{-\beta_r t}.$$

The resulting model describes well the relative frequency of aNSCs as a fraction of all NSCs the decline of which provides the best fit to the data displayed in Fig.1H.

To further characterize the increasing quiescence scenario, we can compute the mean time a NSC spends in quiescence during aging. The calculation is based on a corresponding stochastic interpretation of the differential equation model and the property that a random variable, exponentially distributed with parameter $r$, has mean $1/r$. The resulting mean time in quiescence, $1/r(t)$, is displayed in Data S1-Fig.3.

## 4.4 Comparison of the fits: Model selection using Akaike information criterion.

To substantiate our observations that only increasing quiescence can explain the data, we make use of model selection theory by computing Akaike information criterion (AIC) weights for each of the discussed scenarios (Data S1-Tables 1, 2 and 3). The level of empirical support of a certain model is considered substantial if $0 \leq \Delta \leq 2$, considerably less so if $4 \leq \Delta \leq 7$ and none, if $\Delta > 10$ holds (Burnham and Anderson, 2002). The obtained Akaike weights for all fitted models are displayed in Section 6. Thus, model selection theory also suggests that only the increasing quiescence scenario, i.e. increasing the mean time a cell spends in the quiescence, fits to the data.

## 4.5 Comparison of the fits: Model with two time-dependent parameters.

To further validate our result and discriminate between the two age-dependent scenarios, we consider a model combining the two time-dependent parameters describing increasing frac-

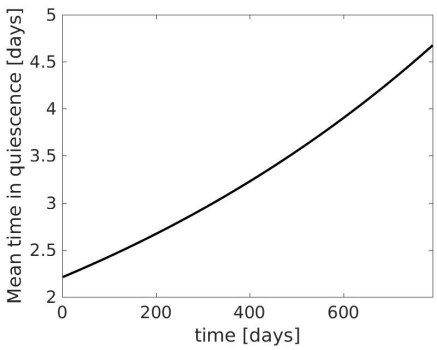


Data S1-Fig. 3: Predicted mean time NSC spends in the quiescent phase depending on the age of the animal. The prediction is based on the increasing quiescence scenario.

tion of self-renewal and increasing the mean time a cell spends in the quiescence, simultaneously. Obviously, increasing the number of free parameters allows finding a fit with a smaller weighted sum of squared residuals; see Data S1-Fig.5, Fig.7 and Fig.12 compared in Data S1-Fig.16. However, it is not a better fit in terms of the Akaike Information Criterion (AIC), which measures goodness-of-fit taking into account the number of degrees of freedom involved. To weight the contribution of time-dependent changes in the two parameters, we compare their estimated dynamics; see Data S1-Fig.17. We see that the optimal fit of the model with two time-dependent parameters resembles the scenario involving the time-dependent quiescence only, i.e. it requires that the rate of activation from quiescence significantly decreases in time and that the self-renewal fraction remains nearly constant in time (changing slightly only at younger ages), while it is very different from the fit with only self-renewal increasing in time. This comparison of the estimated cell properties shows that even if the two parameters undergo age-dependent changes, it is the time-increasing quiescence (decreasing rate of activation from quiescence) which is the major component of the regulatory process and allows explaining the observed dynamics.

# 5 Fraction of active label-retaining cells

In order to simulate the fraction of active label-retaining cells, mathematical insights have to be utilized: The protocol used for measuring active label-retaining cells was administration of

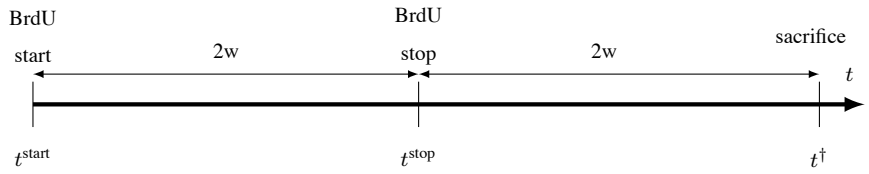


Data S1-Fig. 4: Experimental protocol for the analysis of active label-retaining cells. Animals had access to BrdU-dilluted drinking water for two weeks. Two weeks after stopping BrdU administration, animals were sacrificed and label-retaining cells analyzed (data shown in Figs S1 C-D, Fig.S5)

BrdU in drinking water for two weeks followed by a two week waiting period before animal sacrifice (Data S1-Fig.4).

At the time of sacrifice, the fraction of Ki67$^+$BrdU$^+$ cells among all BrdU$^+$ cells is comprised of aNSCs and progenitors:

$$\frac{Ki67^+BrdU^+cells}{BrdU^+cells}(t=t^\dagger) = \frac{BrdU^+aNSC + BrdU^+prog}{BrdU^+qNSC + BrdU^+aNSC + BrdU^+prog}(t=t^\dagger). \tag{5.1}$$

Moreover, the ratio of aNSCs to qNSCs at the time of sacrifice mirrors the ratio of $BrdU^+$ aNSCs to $BrdU^+$ qNSCs at that time, since during the two week waiting period between BrdU stop and sacrifice, a quasi steady-state among $BrdU^+$ cells is achieved:

$$\frac{BrdU^+aNSC}{BrdU^+qNSC}(t=t^\dagger) = \frac{aNSC}{qNSC}(t=t^\dagger). \tag{5.2}$$

Putting (5.1) and (5.2) together, we obtain

$$\frac{Ki67^+BrdU^+cells}{BrdU^+cells}(t=t^\dagger) = \frac{\frac{aNSC}{qNSC} + \frac{BrdU^+prog}{BrdU^+qNSC}}{1 + \frac{aNSC}{qNSC} + \frac{BrdU^+prog}{BrdU^+qNSC}}(t=t^\dagger).$$

Thus, in order to compute the fraction of $Ki67^+$ cells among all $BrdU^+$ cells at the time of sacrifice, we need to compute $\frac{BrdU^+prog}{BrdU^+qNSC}(t=t^\dagger)$, since the ratio $\frac{aNSC}{qNSC}(t=t^\dagger)$ can be obtained from the solution of the differential equation model (1.1). The ratio $\frac{BrdU^+prog}{BrdU^+qNSC}(t=t^\dagger)$ cannot be obtained from the differential equation. The reason is that any $prog_n$ cell being produced prior to the time point $t=t^\dagger-(n+2)t_c^{\text{prog}}$ would have already become a neuroblast at $t=t^\dagger$, but according to the differential equation, a large number of $prog_n$ cells being born prior to $t=t^\dagger-(n+2)t_c^{\text{prog}}$ would remain at $t=t^\dagger$. Individual-based behavior involving a deterministic

conversion of one cell type to another after a fixed amount of time cannot be simulated in the framework of differential equations. However, the ratio $\frac{BrdU^+prog}{BrdU^+qNSC}(t = t^\dagger)$ can be evaluated as follows:

$BrdU^+$ progenitors at the time of sacrifice can only originate from $BrdU^+$ qNSCs that exist at the time where BrdU is stopped being added to the drinking water, because any qNSCs becoming activated at an earlier time would lead to progenitors that, at the time of sacrifice, would already have become neuroblasts that migrated away from the SVZ. If a qNSCs existing at the time of discontinuing BrdU becomes an aNSCs at a time between $t = t^\dagger - (n+1-k)t_c^{prog} - t_c^{stem}$ and $t = t^\dagger - (n-k)t_c^{prog} - t_c^{stem}$ $(k = 0, \dots, n)$, then one $t_c^{\text{stem}}$ later, this aNSC gives rise to two $\text{prog}_0$ cells with probability $1 - b$ and a further $(n - k)$ $t_c^{\text{prog}}$ later, $2 \cdot 2^{n-k}$ $prog_k$ progenitors exist at a time between $t = t^\dagger - t_c^{prog}$ and $t = t^\dagger$. This reasoning can be summarized as follows:

- $t(BrdU^+qNSC \to BrdU^+aNSC) \in [t^\dagger - (n+1-k)t_c^{prog} - t_c^{stem}, t^\dagger - (n-k)t_c^{prog} - t_c^{stem}]$

$\Rightarrow$ $t(\text{birth of } 2prog_0) \in [t^\dagger - (n+1-k)t_c^{prog}, t^\dagger - (n-k)t_c^{prog}]$ w. prob. $(1-b)$

$\Rightarrow$ $t(\text{birth of } 2^{n-k+1}prog_k) \in [t^\dagger - t_c^{prog}, t^\dagger]$ w. prob. $(1-b)$

Let $\mathcal{P}(x)$ denote the probability of event $x$. It holds

$$\begin{aligned}&\mathcal{P}\Big(t(BrdU^+qNSC \to BrdU^+aNSC) \in [t^\dagger - (n+1-k)t_c^{prog} - t_c^{stem},\ t^\dagger - (n-k)t_c^{prog} - t_c^{stem}]\Big)\\ &= e^{-r\left(t^\dagger - (n-k)t_c^{prog} - t_c^{stem}\right)}\left(e^{rt_c^{prog}} - 1\right).\end{aligned}$$

This equality holds because, as explained above, the time until a qNSCs becomes an aNSCs is exponentially distributed with parameter $r$ and it holds that

$$\mathcal{P}(X \in [t_1, t_2] \mid X \sim \text{exp}(r)) = e^{-rt_1} - e^{-rt_2}.$$

The expected number of $\text{BrdU}^+$ stem cell activations in the time interval $[t^\dagger - (n+1-k)t_c^{prog} - t_c^{stem},\ t^\dagger - (n-k)t_c^{prog} - t_c^{stem}]$ is then given by $e^{-r\left((n-k)t_c^{prog} - t_c^{stem}\right)}\left(e^{rt_c^{prog}} - 1\right) \cdot BrdU^+qNSC(t = t^\dagger - (n+1-k)t_c^{prog} - t_c^{stem})$.

Taken together,

$$BrdU^{+}prog(t=t^{\dagger})$$
$$=(1-b)\sum_{k=0}^{n}2^{n-k+1}e^{-r\left(t^{\dagger}-(n-k)t_c^{prog}-t_c^{stem}\right)}\left(e^{rt_c^{prog}}-1\right)\cdot BrdU^{+}qNSC(t^{\dagger}-t_c^{stem}-(n-k+1)t_c^{prog})$$

and thus

$$\frac{BrdU^{+}prog(t=t^{\dagger})}{BrdU^{+}qNSC(t=t^{\dagger})}$$
$$=(1-b)\sum_{k=0}^{n}2^{n-k+1}e^{-r\left(t^{\dagger}-(n-k)t_c^{prog}-t_c^{stem}\right)}\left(e^{rt_c^{prog}}-1\right)\frac{BrdU^{+}qNSC(t=t^{\dagger}-t_c^{stem}-(n-k+1)t_c^{prog})}{BrdU^{+}qNSC(t=t^{\dagger})}.$$

# 6 Fitting Results

In the following we present the detailed results of the model fitting. In Section 6.1 we combine the experimental data of active cells among TLX$^+$ cells with the experimental data of active cells among label-retaining cells. This is motivated by taking into account that both experimental approaches target the same cell population and it results in an increased number of data points for the fraction of active NSC. In Section 6.2 we repeat the fitting using solely the fraction of active among label-retaining cells to represent the fraction of active NSC. In Section 6.3 we repeat the fitting using solely the fraction of active among TLX$^+$ cells to represent the fraction of active NSC.

## 6.1 Joined dataset

In this Section we combine the experimental data of active cells among TLX$^+$ cells with the experimental data of active cells among label-retaining cells to increase the number of data points (data shown in Fig.S1 A-D, Fig.S5). Data S1-Table 1 summarizes parameter values and statistical quantities obtained from the fitting of the different model versions. The fits of the neurogenesis model obtained assuming no aging, cell cycle lengthening, increasing self-renewal or increasing quiescence are depicted in Fig.1 E-H of the main text. The fit obtained

if we assume simultaneous increase of quiescence and self-renewal during aging is shown in Data S1-Fig.5.

| Mechanism | Parameters | $R^2$ | $\Delta AIC_c$ |
|---|---|---|---|
| Increasing quiescence and self-renewal | $r_{max} = 0.445\ d^{-1}$<br>$\beta_r = 9.2 \cdot 10^{-4}\ d^{-1}$<br>$b_{min} = 0.489$<br>$\beta_b = 0.0022\ d^{-1}$ | 0.9758 | 0 |
| Increasing quiescence | $r_{max} = 0.453\ d^{-1}$<br>$\beta_r = 9.5 \cdot 10^{-4}\ d^{-1}$<br>$b = 0.494$ | 0.9722 | 1.3 |
| Increasing self-renewal | $r = 0.280\ d^{-1}$<br>$b_{min} = 0.0049$<br>$\beta_b = 0.0276\ d^{-1}$ | 0.9537 | 16.7 |
| No aging | $r = 0.278\ d^{-1}$<br>$b = 0.489$ | 0.9468 | 18.1 |
| Cell cycle lengthening | $r = 0.292\ d^{-1}$<br>$b = 0.489$<br>$p_{max} = 0.996\ d^{-1}$<br>$\beta_p = 1.1 \cdot 10^{-9}\ d^{-1}$ | 0.9468 | 23.7 |

Data S1-Table 1: Summary of fitting results. We have combined the experimental data of active among $TLX^+$ cells and active among label-retaining cells to quantify the fraction of active NSC.

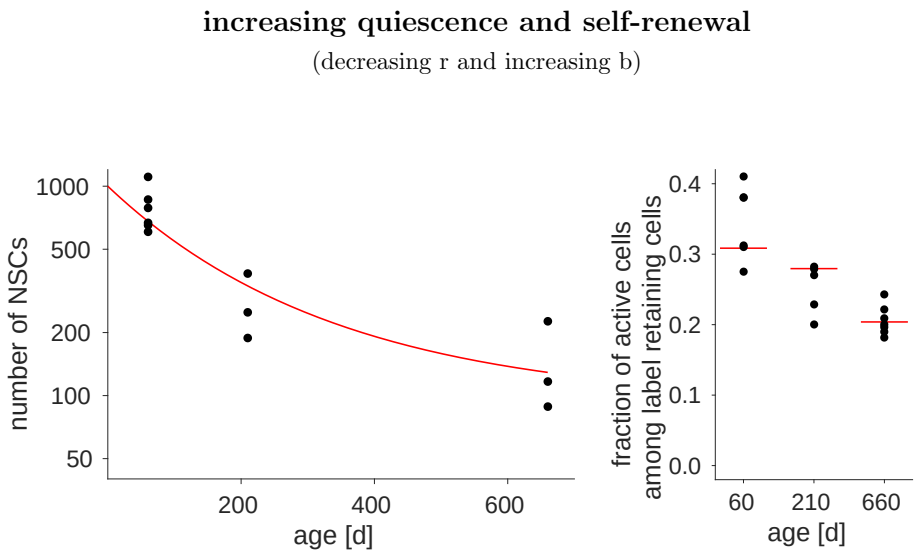


Data S1-Fig. 5: Fit of the neurogenesis model with increase of quiescence and self-renewal during aging. The red curves correspond to model simulations. Each black dot denotes experimental data of one mouse. We have combined the experimental data of active among $TLX^+$ cells and active among label-retaining cells to quantify the fraction of active NSC.

## 6.2 LRC data

In this Section we use the fraction of active cells among label-retaining cells to quantify the fraction of active NSC (data shown in Fig.S1 C-D, Fig.S5). Data S1-Table 2 summarizes parameter values and statistical quantities obtained from the fitting of the different models. The different fits are depicted in Data S1-Fig.6 to Fig.10.

| Mechanism | Parameters | $R^2$ | $\Delta AIC_c$ |
|---|---|---|---|
| Increasing quiescence | $r_{max} = 0.407\ d^{-1}$<br>$\beta_r = 8.1 \cdot 10^{-4}\ d^{-1}$<br>$b = 0.492$ | 0.9928 | 0 |
| Increasing quiescence and self-renewal | $r_{max} = 0.401\ d^{-1}$<br>$\beta_r = 7.8 \cdot 10^{-4}\ d^{-1}$<br>$b_{min} = 0.488$<br>$\beta_b = 0.0023\ d^{-1}$ | 0.9940 | 0.1 |
| Increasing self-renewal | $r = 0.246\ d^{-1}$<br>$b_{min} = 7.6 \cdot 10^{-6}$<br>$\beta_b = 0.025\ d^{-1}$ | 0.9897 | 7.8 |
| No aging | $r = 0.243\ d^{-1}$<br>$b = 0.488$ | 0.9880 | 7.8 |
| Cell cycle lengthening | $r = 0.235\ d^{-1}$<br>$b = 0.487$<br>$p_{max} = 0.919\ d^{-1}$<br>$\beta_p = 3.1 \cdot 10^{-8}\ d^{-1}$ | 0.9880 | 14.4 |

Data S1-Table 2: Summary of fitting results. We have used the experimental data of active among label-retaining cells to quantify the fraction of active NSC.

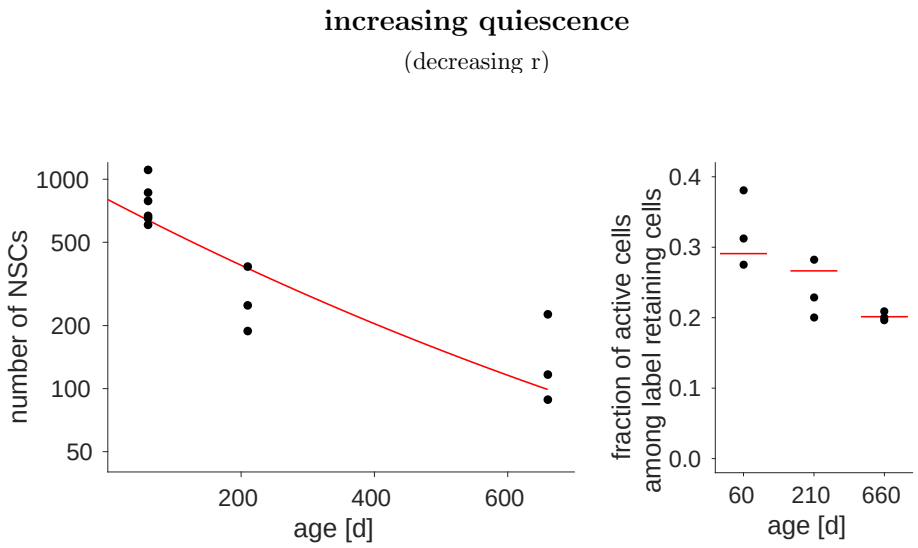


Data S1-Fig. 6: Fit of the neurogenesis model with increase of quiescence during aging. The red curves correspond to model simulations. Each black dot denotes experimental data of one mouse. We have used the experimental data of active among label-retaining cells to quantify the fraction of active NSC.

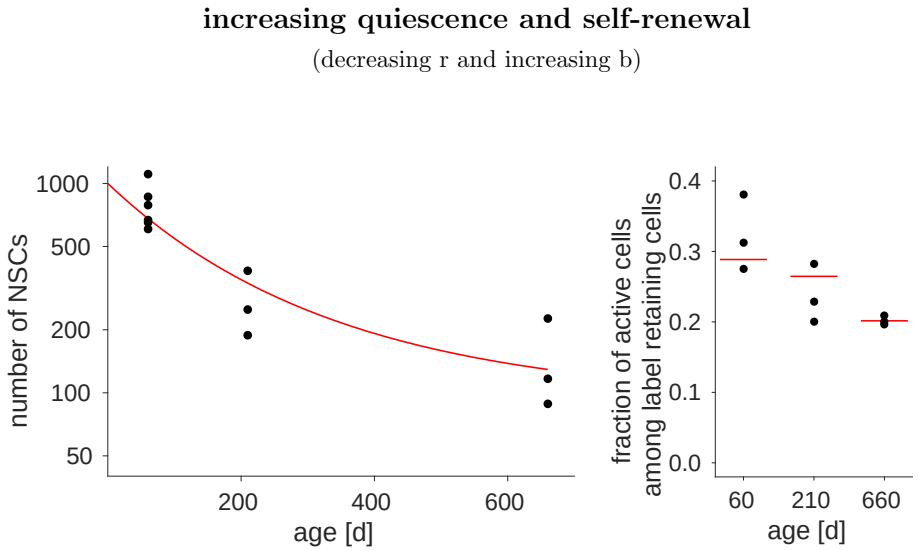


Data S1-Fig. 7: Fit of the neurogenesis model with increase of quiescence and self-renewal during aging. The red curves correspond to model simulations. Each black dot denotes experimental data of one mouse. We have used the experimental data of active among label-retaining cells to quantify the fraction of active NSC.

**increasing self-renewal**

(increasing b)

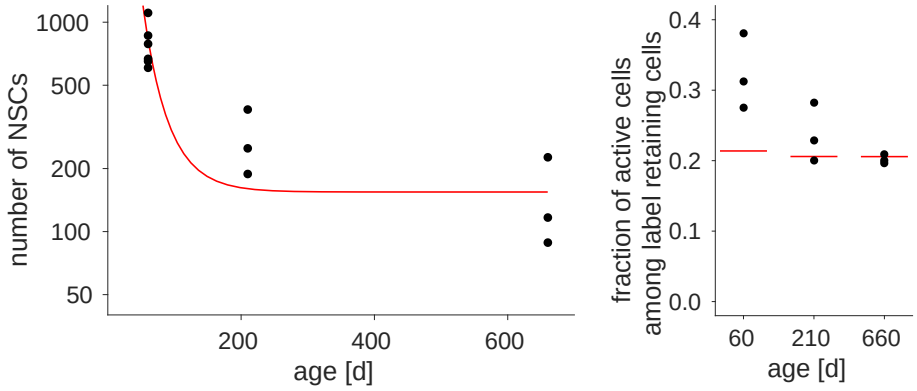


Data S1-Fig. 8: Fit of the neurogenesis model with increase of self-renewal during aging. The red curves correspond to model simulations. Each black dot denotes experimental data of one mouse. We have used the experimental data of active among label-retaining cells to quantify the fraction of active NSC.

**no aging**

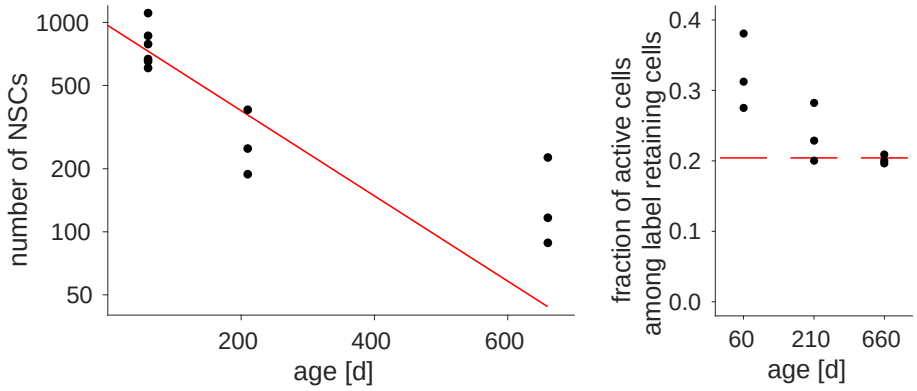


Data S1-Fig. 9: Fit of the neurogenesis model without aging. The red curves correspond to model simulations. Each black dot denotes experimental data of one mouse. We have used the experimental data of active among label-retaining cells to quantify the fraction of active NSC.

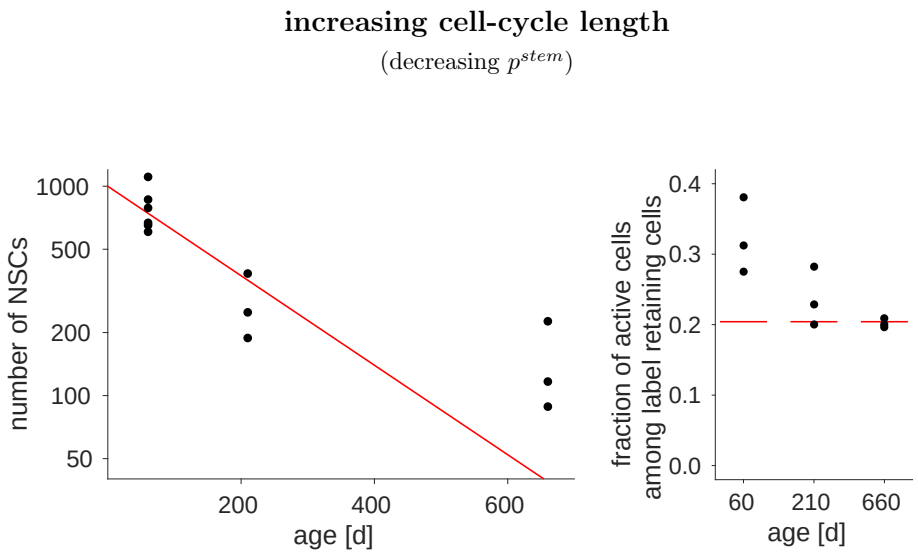


Data S1-Fig. 10: Fit of the neurogenesis model with increase of cell cycle length during aging. The red curves correspond to model simulations. Each black dot denotes experimental data of one mouse. We have used the experimental data of active among label-retaining cells to quantify the fraction of active NSC.

## 6.3 TLX data

In this Section we use the fraction of active cells among $TLX^+$ cells to quantify the fraction of active NSC (data shown in Fig.S1 A-B, Fig.S5). Data S1-Table 3 summarizes parameter values and statistical quantities obtained from the fitting of the different models. The different fits are depicted in Data S1-Fig.11 to Fig.15.

| Mechanism | Parameters | $R^2$ | $\Delta AIC_c$ |
|---|---|---|---|
| Increasing quiescence | $r_{max} = 0.440\ d^{-1}$<br>$\beta_r = 9.3 \cdot 10^{-4}\ d^{-1}$<br>$b = 0.494$ | 0.9937 | 0 |
| Increasing quiescence and self-renewal | $r_{max} = 0.436\ d^{-1}$<br>$\beta_r = 8.9 \cdot 10^{-4}\ d^{-1}$<br>$b_{min} = 0.492$<br>$\beta_b = 0.001\ d^{-1}$ | 0.9939 | 3 |
| Increasing self-renewal | $r = 0.352\ d^{-1}$<br>$b_{min} = 0.093$<br>$\beta_b = 0.028\ d^{-1}$ | 0.9895 | 10.8 |
| No aging | $r = 0.350\ d^{-1}$<br>$b = 0.490$ | 0.9879 | 10.8 |
| Cell cycle lengthening | $r = 0.260\ d^{-1}$<br>$b = 0.487$<br>$p_{max} = 0.706\ d^{-1}$<br>$\beta_p = 6.7 \cdot 10^{-10}\ d^{-1}$ | 0.9879 | 17.4 |

Data S1-Table 3: Summary of fitting results. We have used the experimental data of active among $TLX^+$ cells to quantify the fraction of active NSC.

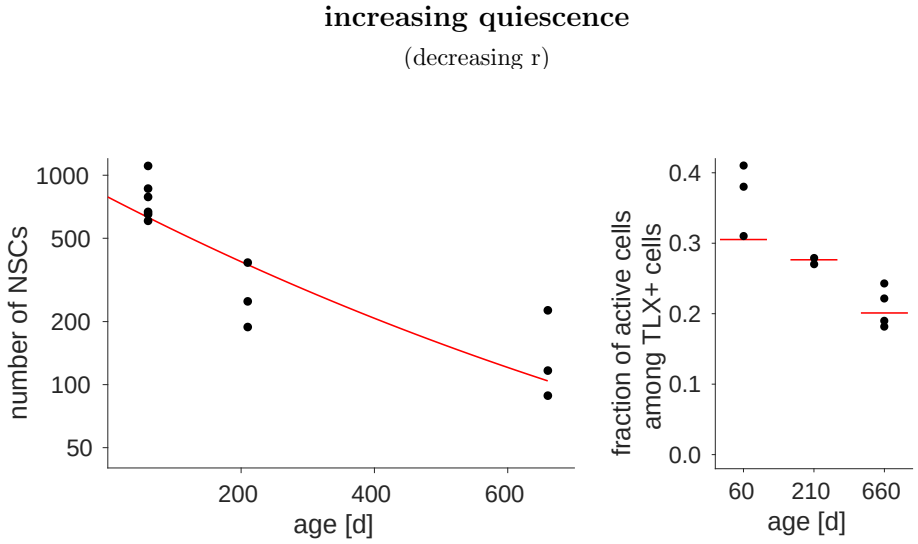


Data S1-Fig. 11: Fit of the neurogenesis model with increase of quiescence during aging. The red curves correspond to model simulations. Each black dot denotes experimental data of one mouse. We have used the experimental data of active among $TLX^+$ cells to quantify the fraction of active NSC.

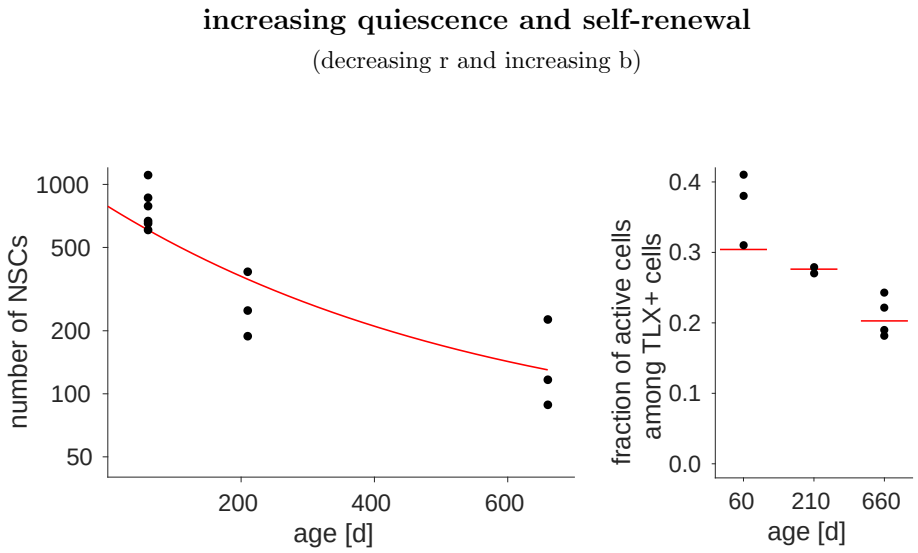


Data S1-Fig. 12: Fit of the neurogenesis model with increase of quiescence and self-renewal during aging. The red curves correspond to model simulations. Each black dot denotes experimental data of one mouse. We have used the experimental data of active among $TLX^+$ cells to quantify the fraction of active NSC.

**increasing self-renewal**

(increasing b)

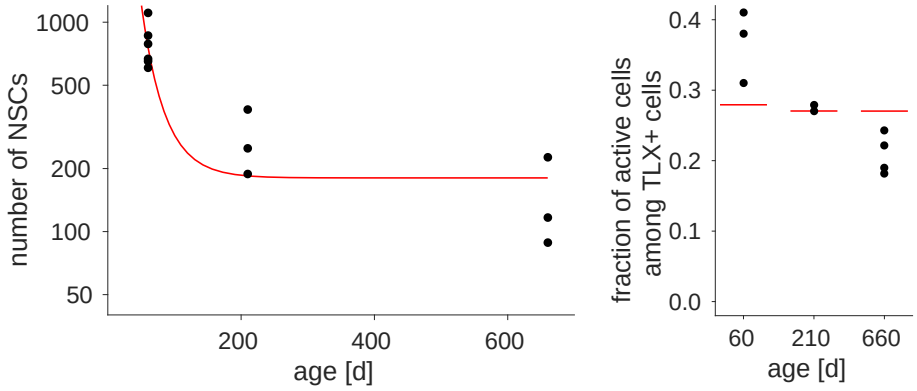


Data S1-Fig. 13: Fit of the neurogenesis model with increase of self-renewal during aging. The red curves correspond to model simulations. Each black dot denotes experimental data of one mouse. We have used the experimental data of active among $TLX^+$ cells to quantify the fraction of active NSC.

**no aging**

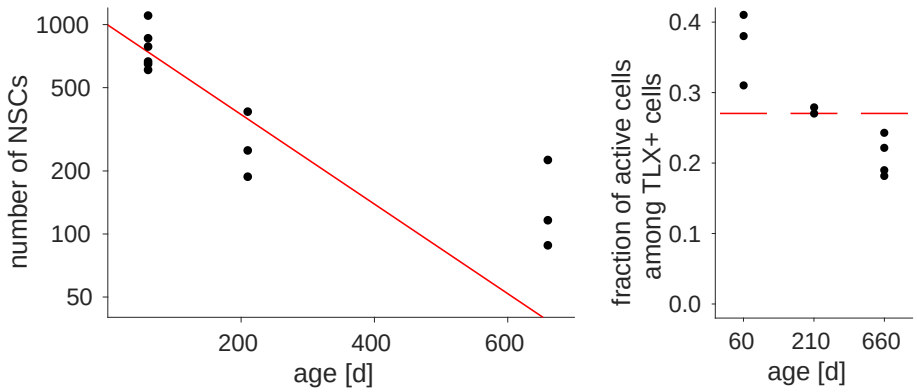


Data S1-Fig. 14: Fit of the neurogenesis model without aging. The red curves correspond to model simulations. Each black dot denotes experimental data of one mouse. We have used the experimental data of active among $TLX^+$ cells to quantify the fraction of active NSC.

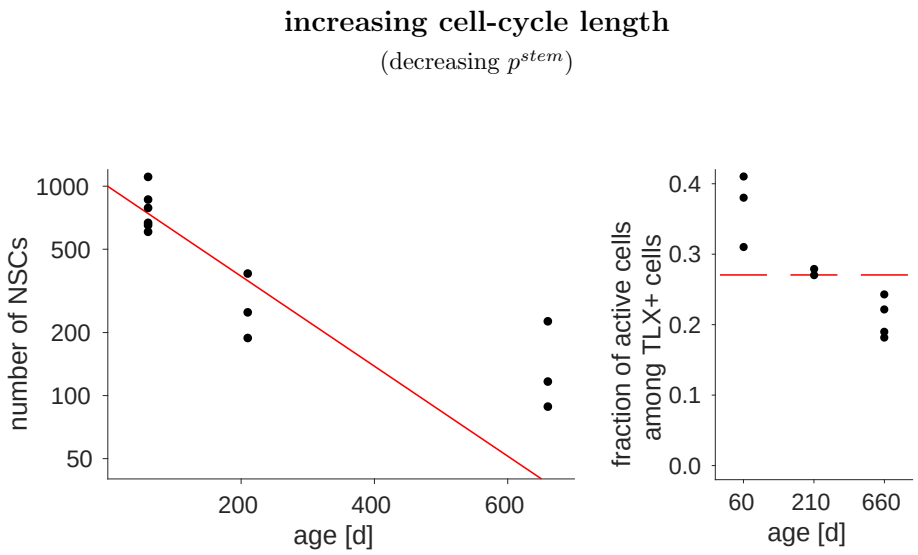


Data S1-Fig. 15: Fit of the neurogenesis model with increase of cell cycle length during aging. The red curves correspond to model simulations. Each black dot denotes experimental data of one mouse. We have used the experimental data of active among $TLX^+$ cells to quantify the fraction of active NSC.

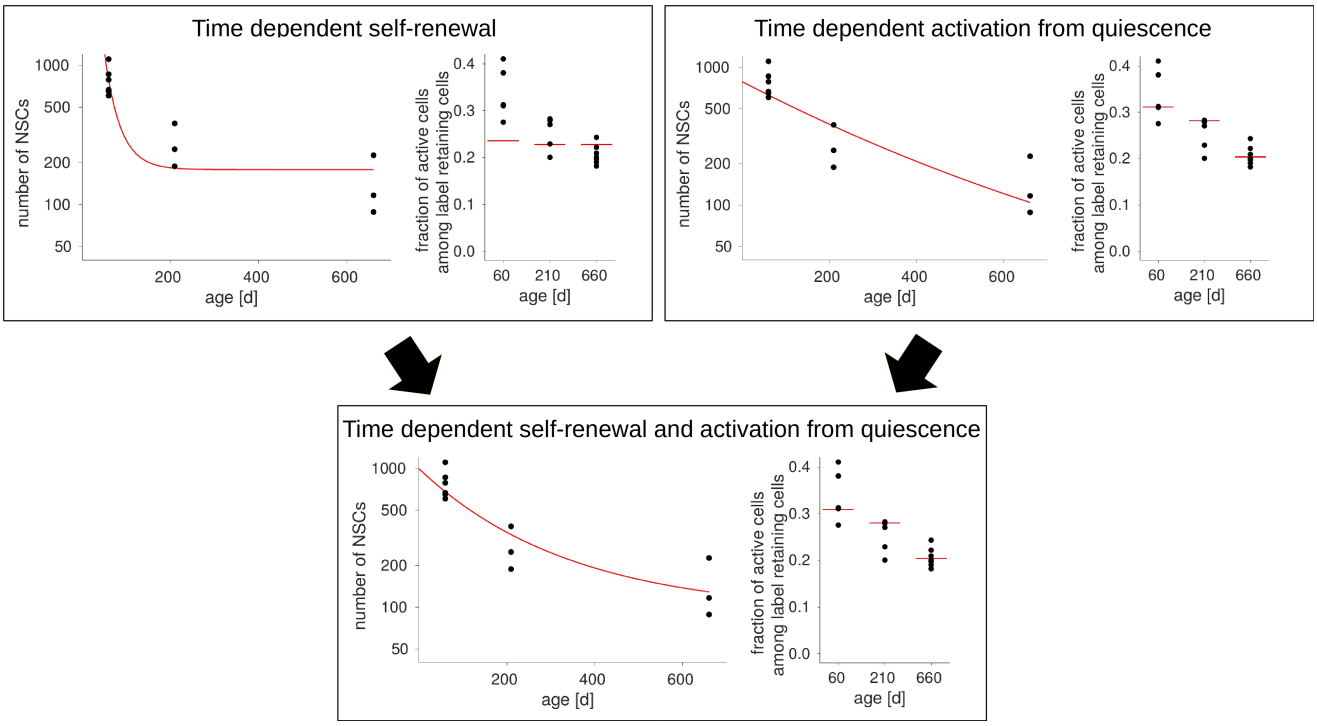


Data S1-Fig. 16: Comparison of the two single time-dependent parameter fits (upper panel) with a fit for a model with two time-dependent parameters (lower panel).

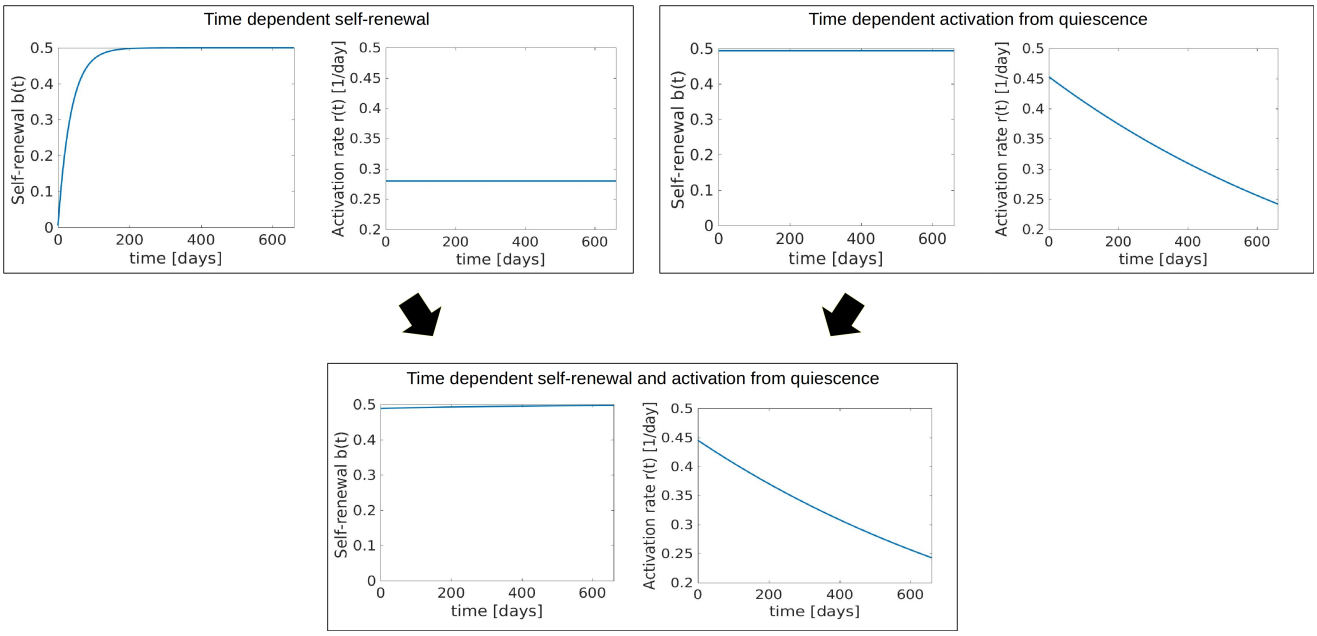


Data S1-Fig. 17: Comparison of the time course of two cell parameters (self-renewal fraction and activation rate) in models with only increasing self-renewal (upper panel left) or only increasing quiescence (upper panel right) versus the model with the two parameters increasing (lower panel).

# Markov chain-based computational method to identify niche determinants:

**Rationale:**

Stem cell-niche interactions involve several diverse and stochastically fluctuating components mediated by different supportive stromal cells, secreted molecules, physical factors such as oxygen tension, shear stress and temperature (Rezza et al., 2014). Such multifactorial complexity of stem cell-niche interactions is a major roadblock in identifying regulatory factors that determine the functional state of the stem cells. Some of these limitations can be overcome by considering that stem cells robustly maintain their state due to a constant effect created by the niche by integrating its signals via signaling pathways (Ravichandran and Del Sol, 2017). Accordingly, a constant niche effect should induce sustained activation/inhibition of specific stem cell signaling pathways in most of the cells within heterogeneous populations exhibiting the same phenotype (niche determinants) (Ravichandran and Del Sol, 2017). This view of stem cell-niche interactions shifts the focus of the problem towards the constant niche effect on key stem cell signaling, instead of accounting for niche composition and its interaction with the stem cells explicitly. Based on this rationale, we propose a novel computational method relying on a Markov chain model of signal transduction for the identification of niche determinants. The method represents a novel way to model sustained signaling mediated by the niche by considering that once the signal from the niche reaches downstream transcription factors, it starts again from the niche in an iterative manner, consequently producing a sustained signal transduction.

**Method description:**

In this modeling framework, signal transduction from the niche to intracellular signaling pathways is modeled as a Markov chain. Here, the signal is represented by a token that moves from one node to another (nodes denote the states of the Markov chain), solely depending on the transition probabilities calculated from experimental data. As depicted in Data S2- Fig. 1A, if the token is at the niche, in the next time step, it can move to any of the three receptor nodes (1, 2 or 3). Further, at each time step, the token moves from the current node to the next node, and eventually reaches the downstream transcription factors. Once the token reaches any of the transcription factor nodes (11 or 12), it starts again to propagate down from the niche (Data S2- Fig. 1). Such a continuous propagation of the token simulates sustained

signaling. Importantly, the stationary probability distribution of the Markov chain provides the steady state probability of a node to contain the token. Those nodes that have high steady state probabilities are more likely to mediate the sustained signal transmission. We have proposed such a Markov-chain model for sustained signal transmission based on the analogy of a token travelling from the receptors to the TFs an infinite number of times. In other words, the token advances from one signaling molecule to the next with certain probability, that is determined by network topology and gene expression of the interacting molecules, and when it reaches a TF it starts again from the niche node. This process can be represented by including a feedback loop from the TFs to the niche node, and therefore the stationary probability distribution of this Markov chain should give the probability for each node to contain the token. In this model, high probability nodes are more likely to mediate the niche induced sustained signal. In addition, the presence of the feedback loop ensures that the stationary distribution does not have all probabilities in the TFs. However, this is a strategy to model the sustained signaling, rather than a biological feedback regulation of the niche by the transcription factors. The steps involved in the computational method are depicted in Data S2- Fig. 2 and an illustrative example of the method is shown in Fig. 6A.

*Method assumptions:*

The method considers that transcript levels measured from sequencing can serve as a surrogate for protein level of the respective gene. Although mRNA levels need not entirely reflect the protein levels due to several other post transcriptional regulatory mechanisms, we believe this assumption is reasonable since we are specifically interested in identifying constantly activated/inhibited signaling intermediates whose steady state protein levels are more likely to have high correlation with the respective steady state mRNA levels (Liu et al., 2016).

*Construction of signaling interactome:*

We combined ReactomeFI (https://reactome.org) and Omnipath (http://omnipathdb.org/) databases and used the resulting compilation as the signaling interactome for our method. These two databases were chosen because they contain information from several other resources and have information of directionality of signal flow and regulatory nature of the interaction. This network consisted of 89444 edges and 5823 nodes. In order to account for the niche influence on the intracellular signaling, we introduced an external niche-node, which we connect to all receptors and ligands in the signaling interactome (Data S2- Fig. 1B).

Since a complete database of receptor/ligand molecules is currently unavailable, to compile a list of receptors/ligands we used Gene Ontology classification of receptor activity and plasma membrane (GO:0004872, GO:0005886) to identify genes with possible receptor activity. Further, in order to model the sustained signaling, we consider that once the signal reaches the transcription factors, it starts once again from the external niche-node. To achieve this, we connected all the transcription factor nodes in the signaling interactome to the external niche-node (Data S2- Fig. 1B). This will ensures a continuous signal transmission from the niche to the transcriptions factors via signaling intermediates. We defined genes as transcription factors/regulators based on the annotation available at Animal TFDB (http://bioinfo.life.hust.edu.cn/AnimalTFDB/). Finally, we removed those nodes that had zero in-degree if they are not a receptor or a ligand and zero out-degree if they are not a transcription factor, as these nodes will not contribute to sustained signal transduction. After filtering for these nodes, the final network consisted of 5299 nodes and 87907 edges.

*Model formulation:*

We model the signal transduction from the niche to intracellular signaling pathways as a finite discrete time-homogenous Markov chain, where the signal originates from the niche and propagates successively via a finite set of signaling molecules $S = \{S_1, S_2, \ldots, S_N\}$. The probability of the signal to propagate from a molecule to another at successive time steps is given by

$$\boldsymbol{P}\big(X(t_{n+1}) = S_j \big| X(t_n) = S_i, X(t_{n-1}) = S_k, \ldots X(t_0) = S_m\big) = \boldsymbol{P}\big(X(t_{n+1}) = S_j \,\big|\, X(t_n) = S_i\big) = p_{ij}$$

Accordingly, if the signal is currently in the molecule $S_i$, the probability of it propagating to molecule $S_j$ at the next time step depends only on where the signal is present in the current time step and not on previous time steps. Here, $p_{ij}$ is the transition probability of the signal to propagate from molecule $S_i$ to $S_j$, defined by the transition probability matrix **P** obtained from the single-cell gene expression data.

Sustained signal transmission is modeled by considering that, once the signal reaches a transcription factor, it is transmitted back to the external niche-node. Since the external niche-node is connected to all receptors and ligands, such a transmission of signal back to niche-node ensures that the signal continuously propagates from the niche to the transcription factors via the signaling intermediates (Data S2- Fig. 1B and Fig. 6A). Further, this ensures that the signaling interactome forms a strongly connected graph where one can reach any node from any other node via a directed path. Consequently, this Markov chain is irreducible

(since the signaling interactome forms a graph with a single strongly connected component) and positive recurrent (since it is irreducible and finite).

*State transition probability matrix:*

For the construction of the state transition probability matrix, we rely on the mass action principle, where we assume that the probability of interaction among two nodes is proportional to the product of the expression values of the corresponding genes. This implies, $p_{ij} \propto E_i E_j$

Accordingly, the transition probabilities are given by,

$$p_{ij} = \frac{w_{ij}}{\sum_{k \in \gamma_i} w_{ik}},$$

where, $\gamma_i$ denotes the set of neighboring molecules regulated by $S_i$ and, $w_{ij}$ denotes the interaction weights defined by

$$w_{ij} = E_i \bullet E_j ,$$

where, $E_i$ and $E_j$ are single cell gene expression vectors for the corresponding genes and $w_{ij}$ is calculated by the dot product (or the scalar product) of the two vectors.

The signaling interactome serves as the topology and determines the interactions for which the transition probabilities are calculated. Therefore, in the transition probability matrix **P**, only those interactions present in the signaling interactome will have a non-zero transition probability calculated from the data and other will have zero probabilities. Further, it should be noted that the matrix **P** is a stochastic matrix.

Single cell expression data generated using SmartSeq2 protocol was used as input for the method to calculate the interaction weights. Further, a gene was considered expressed if it had an FPKM >1 in that cell.

Signal transmission from one molecule to another will depend on their interaction probability derived from single-cell RNA-seq data. For each cellular subpopulation, the interaction probability for any two molecules in the signaling interactome is proportional to the dot product of their expression vectors within the subpopulation. Hence, this probability will be high only when both the molecules are highly expressed in the same cell and expressed in a large number of cells for that subpopulation.

Further, as an independent measure to remove interactions that occur in very few cells, interactions among two intermediates are considered to be present only if both the genes are simultaneously expressed in at least 20% of the cells (i.e. both genes must be expressed in the same cell and in at least 20% of the cells) else the specific interaction is removed from the network.

*Stationary distribution:*

An irreducible, positive recurrent Markov chain has a unique stationary distribution (Stewart, 1994). Once the transition probability matrix is defined, the stationary distribution $\pi$ of the stochastic matrix $\mathbf{P}$ ($\pi P = \pi$), (i.e. the left eigenvector with unit eigenvalue of P) is calculated by finding the eigenvector of transpose of transition probability matrix $\mathbf{P}^t$ with eigenvalue equal to 1 (Stewart, 1994). This distribution gives the steady state probability distribution of where the signal will be present at any given time instant.

*Convergence to a unique stationary distribution*

A finite, irreducible, and aperiodic Markov chain is ergodic, i.e. it has a unique stationary distribution which is equal to the Markov chain's limiting distribution irrespective of the initial conditions (or probability distributions) (Stewart, 1994). We have verified that our construction results in an aperiodic Markov chain. We performed this by considering the lengths of all simple cycles measuring the shortest path lengths from the niche-node and found that the cycle lengths varied from 3 to 7. This ensures that the period of the niche-node, which is defined as the greatest common divisor of all its simple cycles, is 1 because all transcription factors are directly connected to the niche-node. This proves that the Markov chain is aperiodic.

*Identification of subpopulation specific signaling intermediates:*

Based on the method described above, steady state probability distributions for different cell subpopulations in young and old mice are calculated. First, a comparison of these probabilities is made within young or old neural stem cell subpopulations. This will identify those intermediates that are unique to each subpopulation for either young or old mice. As a second step, the resulting list was used for a comparison between young and old mice to identify factors uniquely responsible for the maintenance of the quiescent or active subpopulations in either young or old mice. Table S3 lists the molecules identified for each of

the subpopulations in young and old mice. Data S2- Fig. 3 shows the strategy used to shortlist the potential niche determinants for quiescent neural stem cells for old mice.

*Analyzing the role of key interactions for the observed steady state distributions:*

After calculating the stationary distribution based on the Markov chain, we were interested in contribution of individual interactions for the obtained stationary distribution. For this, we converted the original signaling interactome into a line graph where each node in the line graph is an edge of the original signaling interactome (Data S2- Fig. 4). Product of weights of two edges that interact were used for constructing the transition probability matrix of the line graph. We calculated the stationary distribution of the line graph as mentioned above. This probability distribution denotes the likelihood of an interaction to occur for a given single cell expression data. This information was used to identify the specific interactions uniquely present or absent in old quiescent NSCs when compared to the young ones.

**Data S2 Figure legends**

Data S2- Fig. 1

Panel A: *Representation of signaling as a moving token*. The figure depicts the rationale behind the Markov chain model of sustained signaling. The signal is modelled as a token that moves in the Markov chain (signaling interactome) and is considered to start from the niche and propagate down to the transcription factors. Once the token reaches any of the transcription factor it starts once again from the niche. Such a continuously moving token simulates a sustained signaling from the niche.

Panel B: *A simple representation of the structure of the Markov chain model of the signaling interactome*. The niche-node is connected to all the receptors/ligands and the transcription factors are connected to the niche. These two edges are shown in red color. The green edges are the ones directly obtained from the combined Reactome and Omnipath database.

Data S2- Fig. 2

*Schematic of the steps involved in the computational method for the identification of niche determinants*.

Data S2- Fig. 3

*Schematic of strategy employed to identify niche determinants specific for quiescent neural stem cells in old mice*.

Data S2- Fig. 4

*Schematic of transformation of a normal graph into a line graph*

Data S2 Figure 1

a

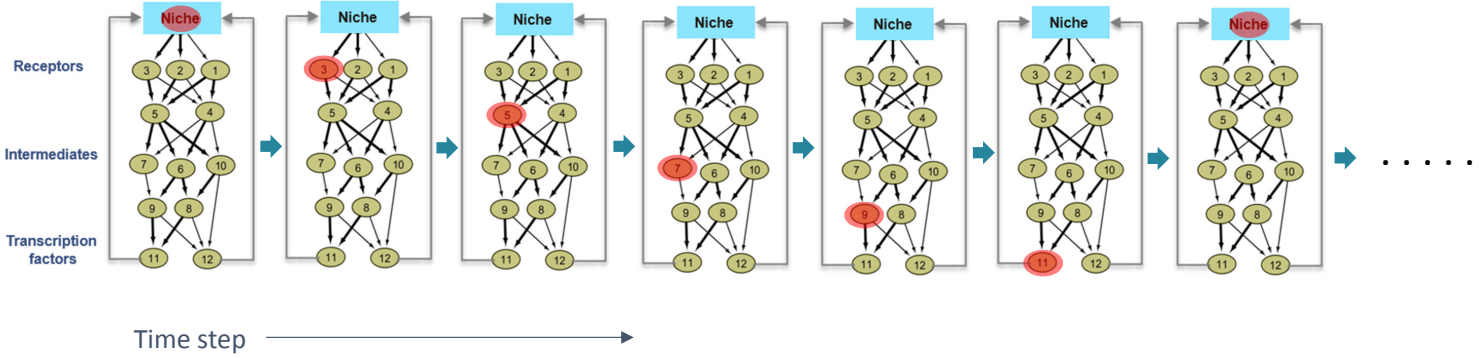


b

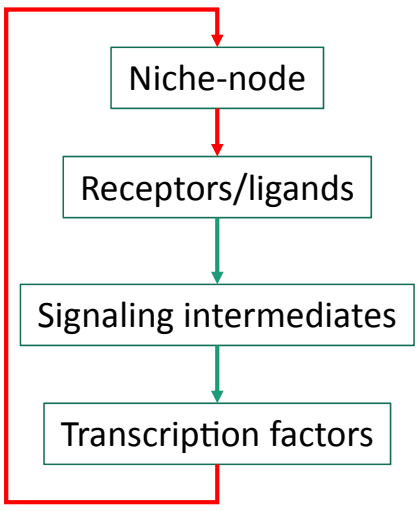

Data S2 Figure 2

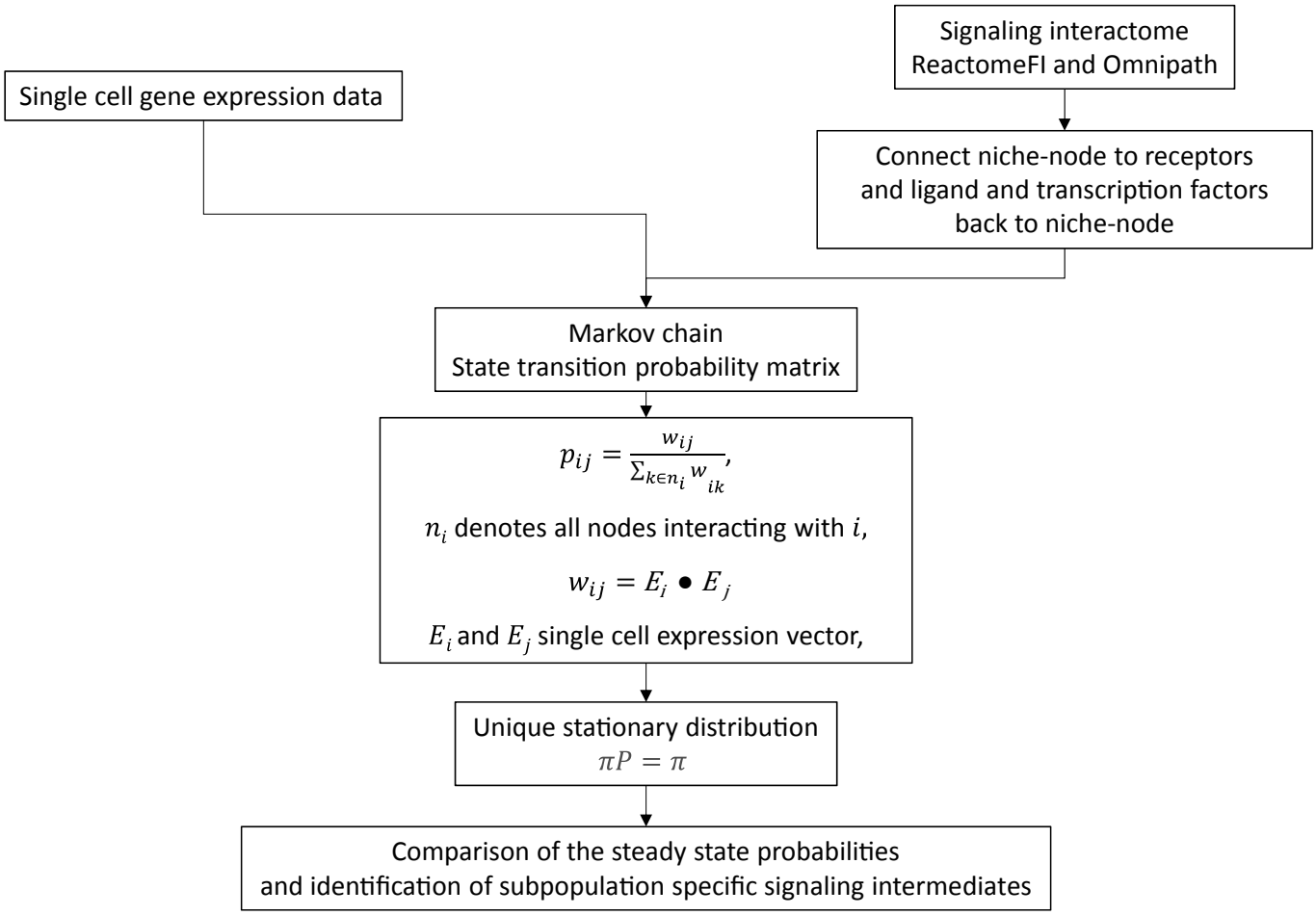

Data S2 Figure 3

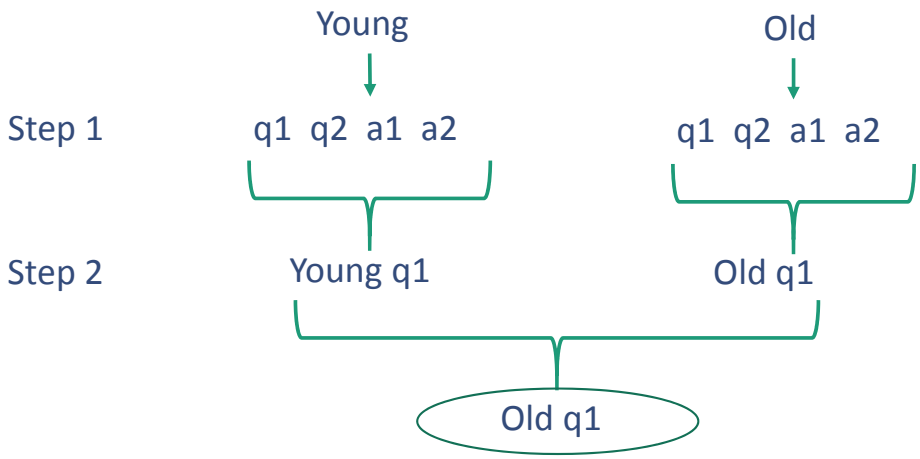

Data S2 Figure 4

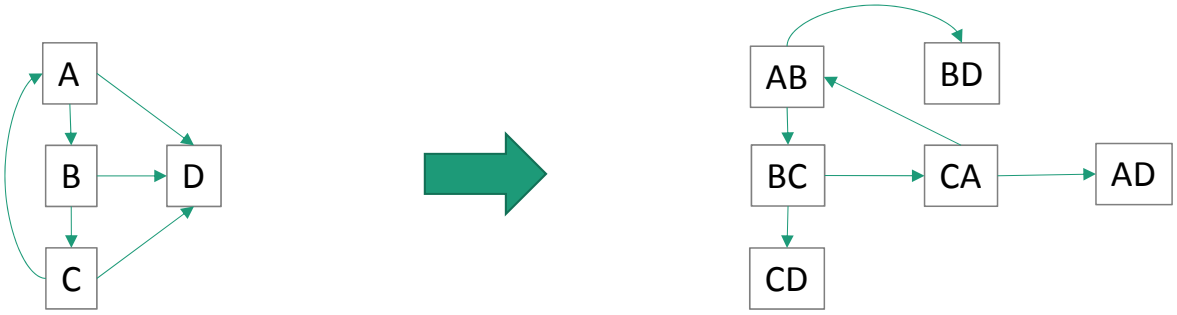


Original graph

Transformed line graph

Supplemental Figure 1

Click here to access/download;Supplemental Figure;FigureS1.jpg

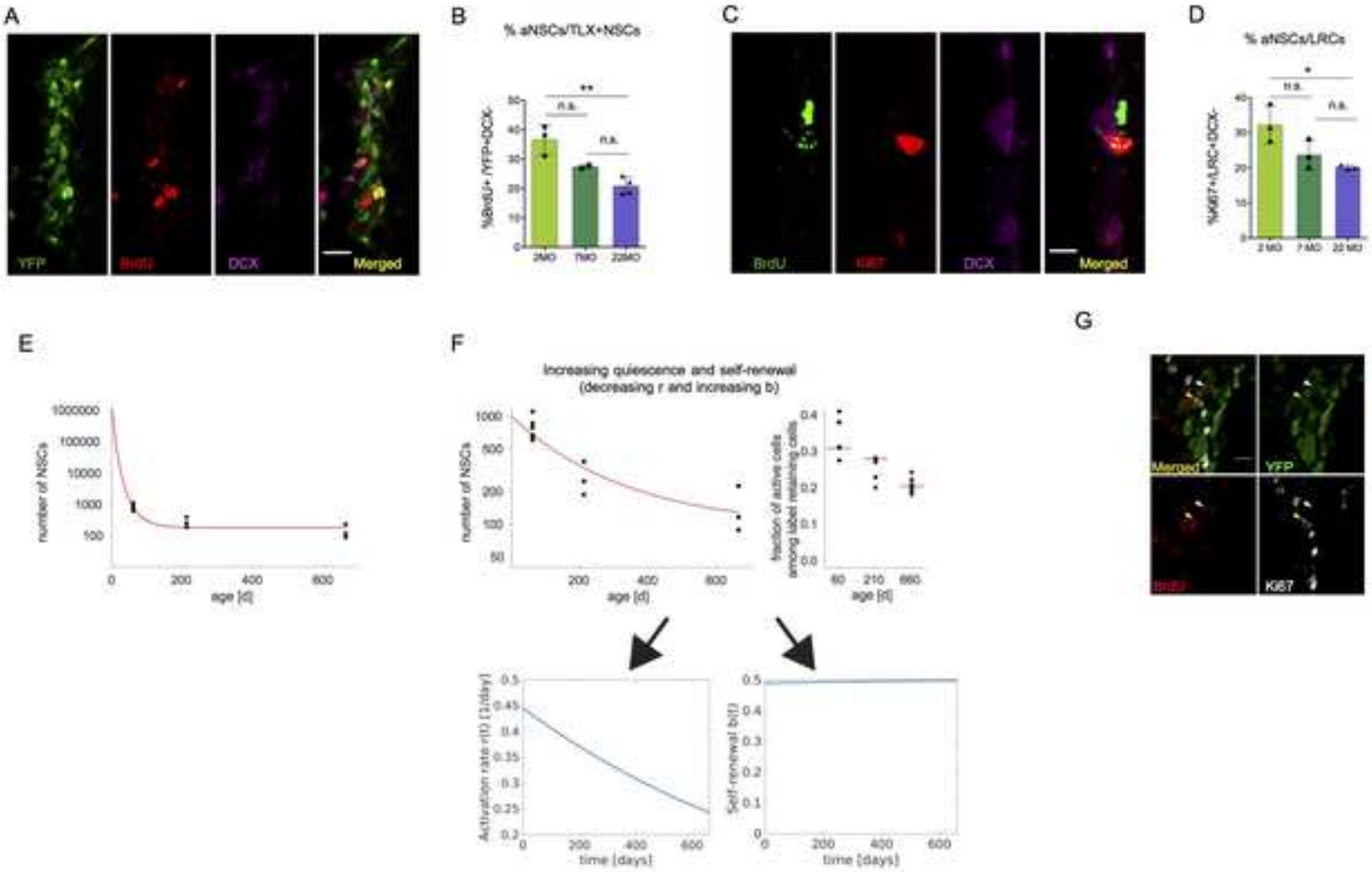

Supplemental Figure2

Click here to access/download;Supplemental Figure;FigureS2.jpg

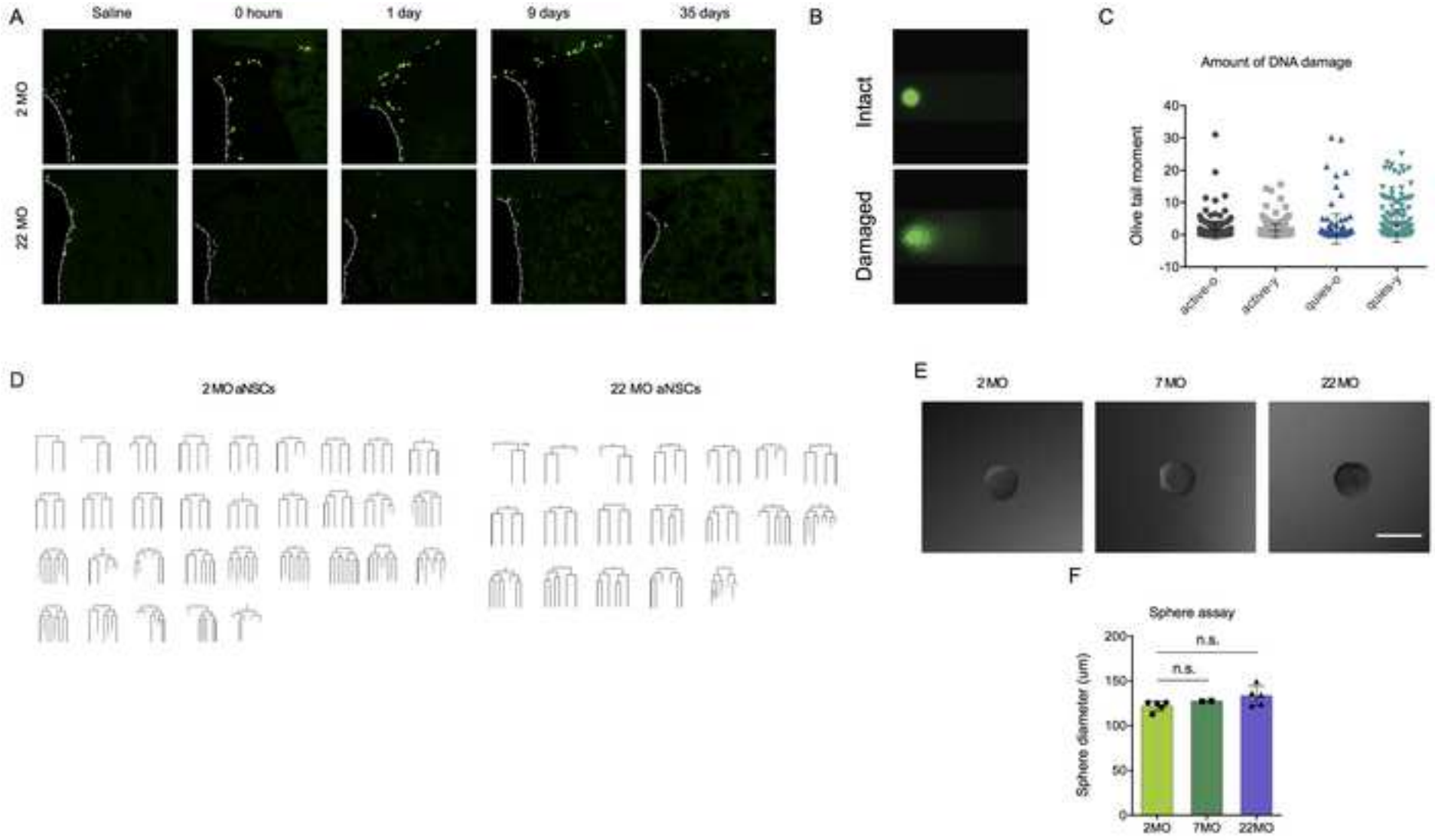

Supplemental Figure3

Click here to access/download;Supplemental Figure;FigureS3.jpg

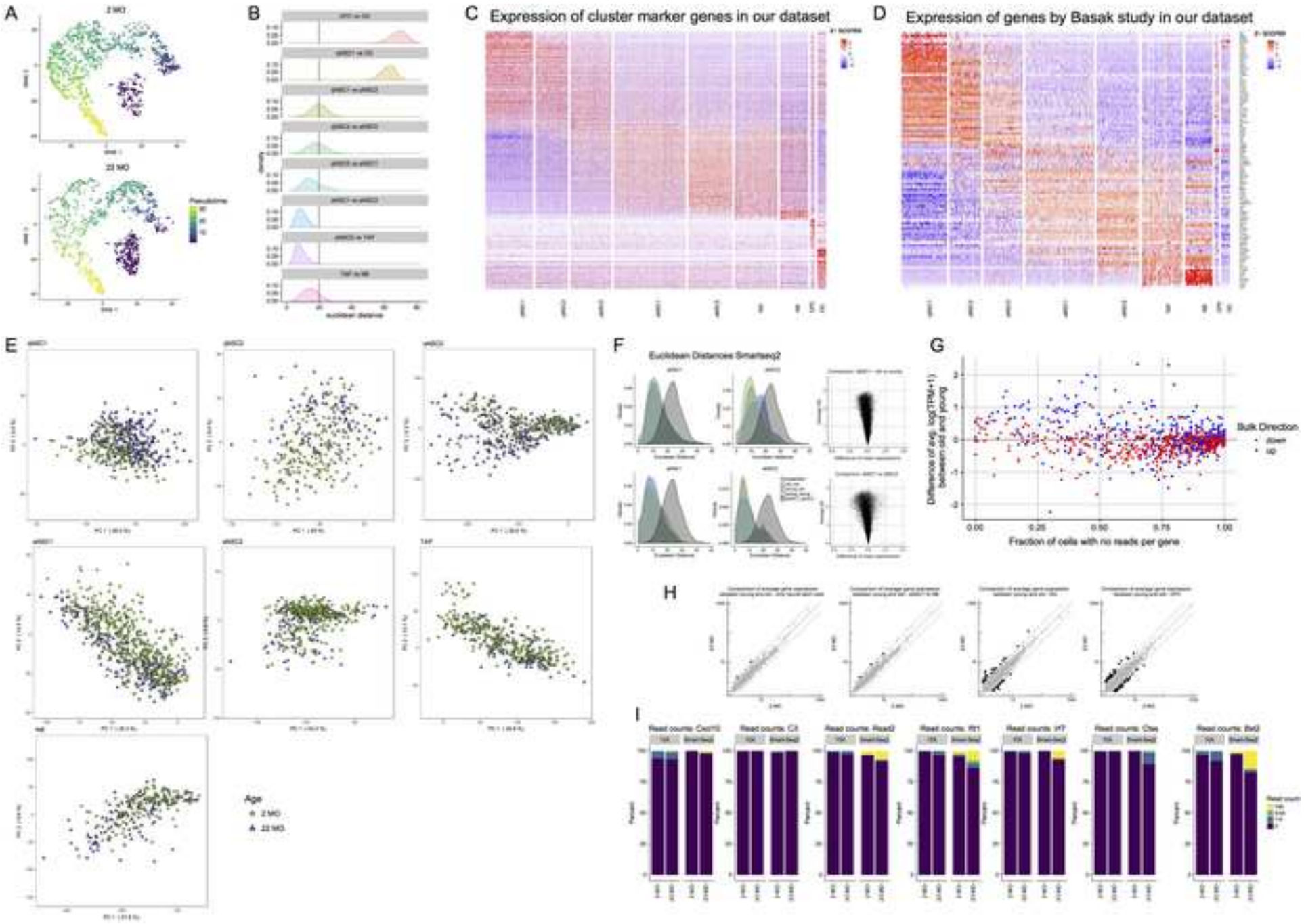

Supplemental Figure4

Click here to access/download;Supplemental Figure;FigureS4.jpg

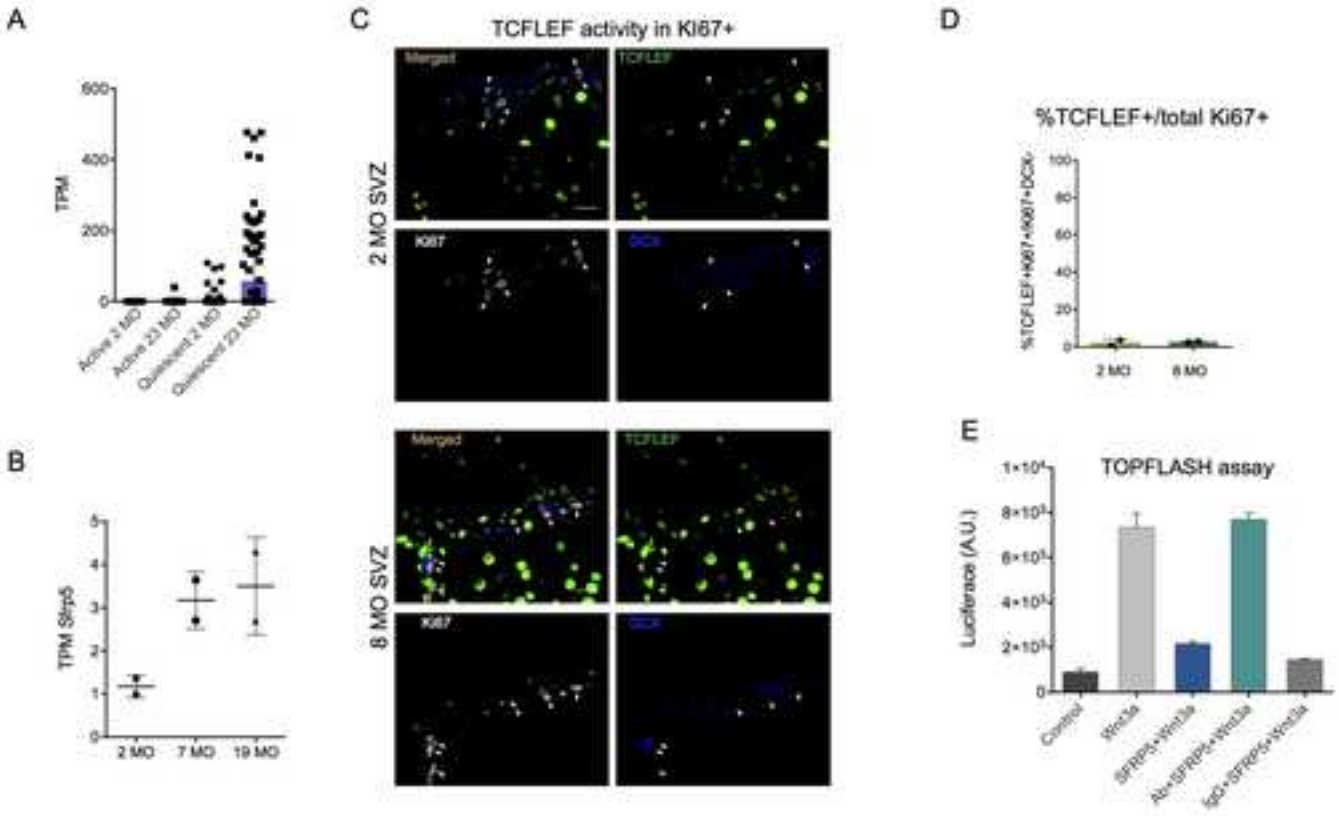

Supplemental Figure5

Click here to access/download;Supplemental Figure;FigureS5.jpg

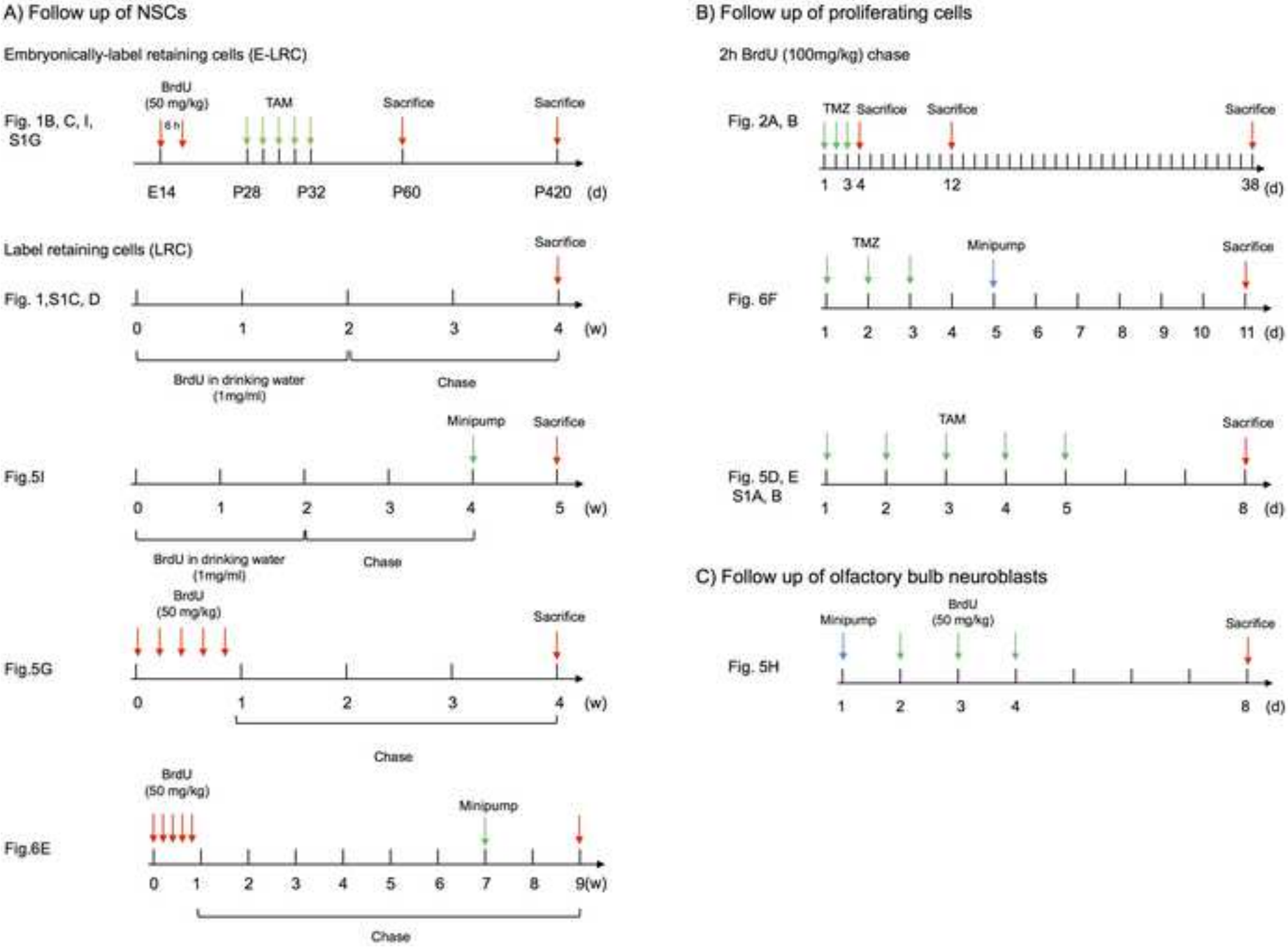

Supplemental Figure6

Click here to access/download;Supplemental Figure;FigureS6.jpg